# Deformation Twinning Versus Slip in Ni-Based Alloys, Containing Pt<sub>2</sub>Mo-Structured, Ni<sub>2</sub>Cr-Typed Precipitates

H.T. Vo<sup>a,co-first</sup>, K. Dang<sup>b,co-first</sup>, F. Teng<sup>c,d</sup>, M. Schneider<sup>b</sup>, B.P. Eftink<sup>b</sup>, S.A. Maloy<sup>b</sup>, J.D. Tucker<sup>d</sup>, L. Capolungo<sup>b,\*</sup>, P. Hosemann<sup>a,\*</sup>

<sup>c</sup>School of Mechanical, Industrial and Manufacturing Engineering, Oregon State University, Corvallis, OR, USA

<sup>d</sup> Characterization and Advanced PIE Division, Idaho National Laboratory, Idaho Falls, ID, USA.

Corresponding author emails: laurent@lanl.gov, peterh@berkeley.edu

#### **Abstract**

Nickel-based alloys are extensively used in a wide range of extreme environments because of their exceptional mechanical properties. The excellent strength of these alloys is derived from the addition of long-range ordered precipitates, introduced by thermal aging. The interaction between the dislocations and LRO precipitates dictate the deformation modes and plastic response in these alloys. While the majority of studies have focused on L1<sub>2</sub>-structured precipitate-strengthened Ni-based alloys, less work has considered the Ni-based alloys containing Pt<sub>2</sub>Mo-structured, Ni<sub>2</sub>(Cr,Mo)-typed precipitates. In these alloys, Pt<sub>2</sub>Mo-structured precipitates enable room-temperature deformation twinning in addition to slip, which increases strain hardenability measured from bulk mechanical testing. Although previous geometric-based model suggested that deformation twinning is favored over slip, the factors that influence the activation between twinning versus slip have not been thoroughly explored in this class of Ni-based alloys. In this work, molecular dynamics examined the possible types of dislocation and Pt<sub>2</sub>Mo-structured precipitate interaction at low temperature. Combined with *in situ* micromechanical testing, the role of resolved shear stresses on dislocation partials were

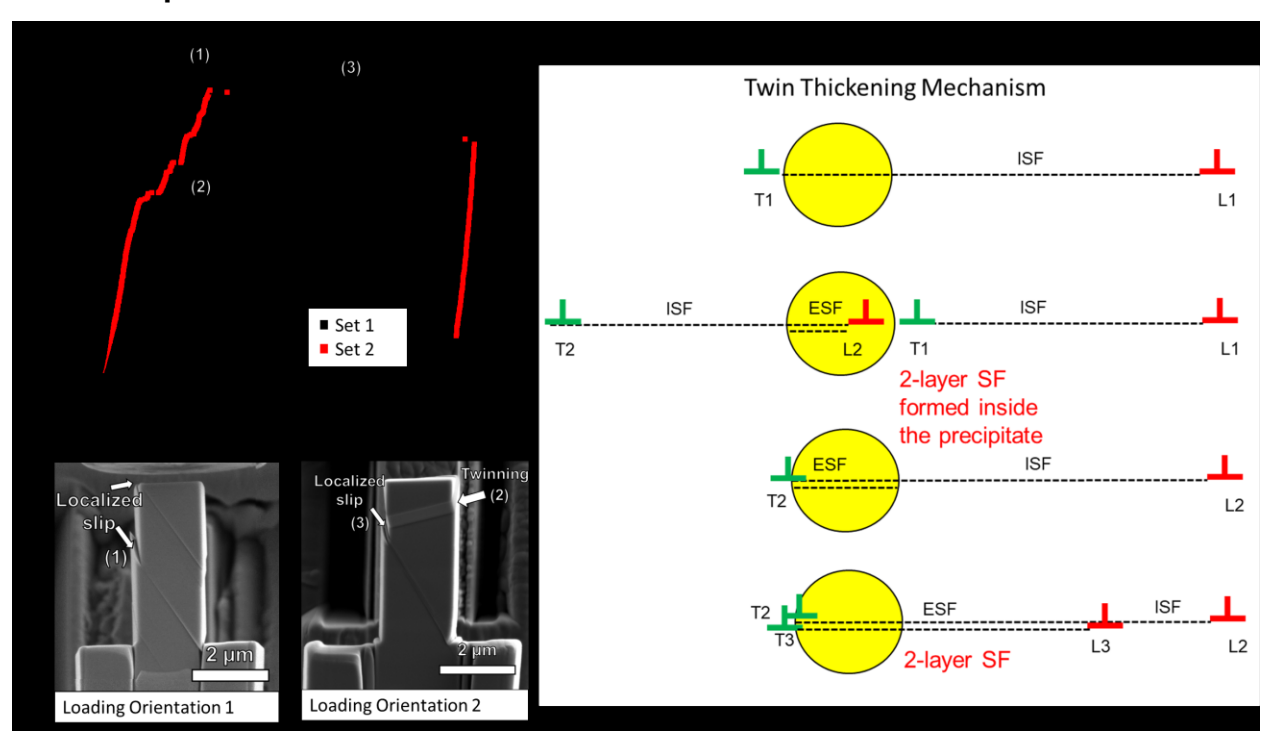
<sup>&</sup>lt;sup>a</sup> Department of Nuclear Engineering, University of California, Berkeley, CA, USA.

<sup>&</sup>lt;sup>b</sup> Los Alamos National Laboratory, Materials Science Division

<sup>\*</sup>corresponding authors

shown to directly influence the activation of slip versus twinning. Additionally, using an energy-based approach, molecular dynamics results demonstrated a novel twin formation process, caused by the dislocation interaction with the Pt<sub>2</sub>Mo-structured precipitates.

## **Graphical Abstract**



**Keywords:** Nickel-based alloys; deformation twinning; micromechanical testing; atomistic simulations; dislocations; ordered precipitates

#### 1. Introduction

Nickel-based alloys are known to offer an exceptional combination of high temperature strength, toughness, creep resistance, and corrosion resistance in highly corrosive environments [1–3]. These alloys are widely used for high temperature applications such as in jet engines [4], electrical power-generation turbines [5,6], and nuclear power plants [7,8]. Their complex chemical compositions provide precipitate strengthening through the addition of Ti, Cr, Al; corrosion resistance, through the addition of Al, Cr; and creep resistance through the addition of Re, W, Mo [3]. For strength improvement, thermal aging is used to introduce both long-range ordered (LRO) and short-range ordered (SRO) precipitates into the materials to increase dislocation pinning [9]. Ordered precipitates increase dislocation resistance via two well-understood phenomena: Orowan strengthening and anti-phase boundary strengthening [10-12]. Orowan strengthening can be described by a range of strength hardening laws such as dispersed barrier hardening (DBH) [13] and Bacon-Kocks-Scattergood (BKS) model [14]. Anti-phase boundary (APB) strengthening results from the additional energy required by a dislocation crossing the boundary to disrupt the order of the precipitates [10]. The mechanism of APB strengthening depends on the structure of the ordered precipitate. For example, for shearable L<sub>12</sub> precipitates (e.g. Ni<sub>3</sub>Al), dislocations travel in pairs to shear the ordered precipitates. The first dislocation creates an APB while the second dislocation restores the order [12,15-18]. The repetitive APB creation due to the dislocation pair shearing increases the strength of nickel-based alloys containing L12-structured precipitates such as Ni<sub>3</sub>Al [17]. Although ordered precipitates play a crucial role in increasing the alloy's strength, ordered precipitates can exacerbate plastic instability via slip localization [17,19–24], which can reduce the materials' ductility. This can result from the glide plane softening mechanism whereby the ordered precipitates become locally disordered and/or dissolved after successive dislocation shearing events [17,19–24]; this local behavior can lead to high strain localization.

Another important aspect of the dislocation and LRO-precipitate interaction is the precipitate-induced deformation twinning, which has been observed to take place in different nickel-based alloys. Most notably, thermally-activated microtwinning in widely-used nickel-based alloys containing Ni<sub>3</sub>Al-based, L1<sub>2</sub>-structured precipitates, have been observed and extensively studied at the intermediate temperatures (650-800° C

depending on the Ni-based alloys) [25,26]. However, a much less-understood deformation twinning mechanism is reported in Ni-Cr and Ni-Cr-Mo type alloys containing Pt<sub>2</sub>Mo-structured precipitates (such as Ni<sub>2</sub>Cr, Ni<sub>2</sub>Mo precipitates). Room temperature bulk mechanical testing of these alloys have shown strong hardening response as a function of aging time and temperature without substantial loss of ductility [27–32]. Transmission Electron Microscopy (TEM) studies reveal that deformation occurs predominantly via slip in the unaged alloys, while mechanical twinning is active and more dominant in the aged alloys, containing Pt<sub>2</sub>Mo-structured precipitates [28–32]. From these works, it was proposed that the Pt<sub>2</sub>Mo-structured precipitates promote mechanical twinning; thus, enhancing the ductility of the Ni-based alloys. In general, the role of mechanical twinning in increasing ductility, fracture toughness, and strength has been shown in many different classes of alloys [33,34], so it is not surprising to see similar strengthening mechanisms are activated in these Ni-based alloys. What remain unclear are the various factors influencing the activation of deformation twinning versus slip and the Pt<sub>2</sub>Mo—structured precipitate-induced deformation twinning mechanism. In this study, we discussed the roles of the orientation relationship (OR) between the Pt<sub>2</sub>Mo-structured precipitates and the matrix, OR variants, grain orientations as well as Schmid factors of dislocation partials on influencing the competition of twinning versus slip in this class of Ni-based alloys.

To isolate the effect of LRO precipitates on deformation mechanisms, we utilized small scale mechanical testing (SSMT) via *in situ* SEM microcompression. With the rise of miniaturization of devices [35], small scale mechanical testing has been developed for the quantification of the mechanical responses for microscale and nanoscale material volumes [36–44]. It has proven to be an effective technique to study various fundamental deformation mechanisms such as material size effects [37,40,41,45–52], plastic instabilities (strain burst) [45,53–57], grain size effects [51,58,59], and others. In our study, microcompression testing coupled with transmission electron microscopy (TEM) were used to obtain direct observation of the activation of different deformation modes (slip versus twinning) as the orientations are varied. Additionally, molecular dynamics simulations were performed to examine the different types of interactions between the dislocations and Pt<sub>2</sub>Mo-structured precipitates as well as the twin formation process from an energy-based perspective. Given the technological importance of the Ni-Cr and Ni-Cr-

Mo type alloys in the nuclear power industry and other applications [60,61], our work provides useful insights into the physical mechanisms behind the activation of different deformation modes for the nickel-based alloys containing Pt<sub>2</sub>Mo-structured precipitates.

## 2. Theory

The Pt<sub>2</sub>Mo-structured precipitates exist in NiCr- and NiCrMo-based alloys as long-range ordered (LRO) Ni<sub>2</sub>Cr-type and Ni<sub>2</sub>(Cr,Mo)-type precipitates, respectively [27,30,31,62]. In this study, we specifically examined the LRO Ni<sub>2</sub>Cr-type precipitates in a model NiCr alloy with the compositional Ni:Cr ratio of 2:1. The Pt<sub>2</sub>Mo structure is body-centered orthorhombic with Immm symmetry. The OR relationship between the LRO Pt<sub>2</sub>Mo-structured, Ni<sub>2</sub>Cr-type precipitates and the disordered FCC matrix is shown in Figure 1. The OR relationship consists of six different variants. Multiple variants are shown to coexist with homogenous distribution [62–64]. Table 1 outlines the OR for all the six variants with respect to the disordered FCC matrix.

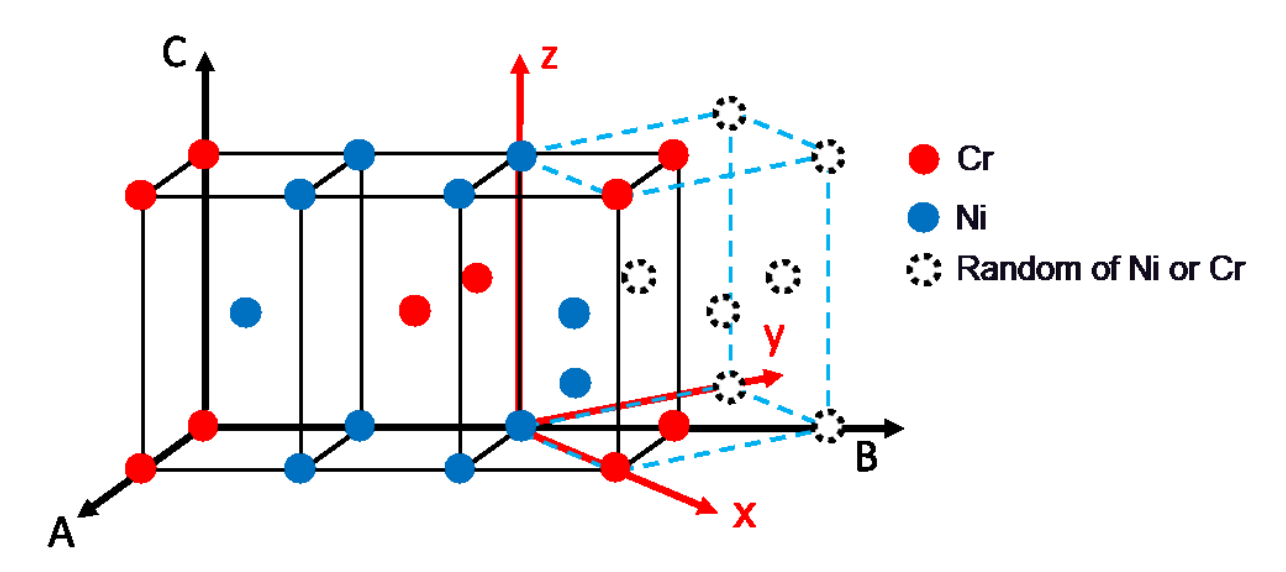


Figure 1. The OR relationship between the disordered FCC matrix and the  $Pt_2Mostructured$ ,  $Ni_2Cr$  type. x-, y-, z-axes corresponding to the [100], [010], and [001] of the FCC matrix. A-, B-, C-axes correspond to the orientations of the precipitate structure. For variant 1, the A-, B-, C-axes are  $[1\bar{1}0]$ , [110], and [001], respectively.

Table 1. The variants of the OR between the Pt₂Mo-structured phase and the disordered FCC matrix [62]. The A, B, C-axes correspond to the orientations of the precipitate structure shown in Figure 1.

Variant Number	Orientation of axes of Pt <sub>2</sub> Mo-structured phase with respect to the disordered FCC matrix				
	A-axis	B-axis	C-axis		
1	[110]	[110]	[001]		
2	[110]	$[1\overline{1}0]$	[001]		
3	[101]	$[10\overline{1}]$	[010]		
4	$[10\overline{1}]$	$[\bar{1}0\bar{1}]$	[010]		
5	[011]	[011]	[100]		
6	[011]	[011]	[100]		

The crystallographic relationship between the FCC slip systems and the LRO Pt<sub>2</sub>Mo-structured precipitates is shown in Figure 2 for variant 1. For each OR variants, we found that 10 out of 12 slip systems cause formation of ABP as the dislocation shearing disrupts the precipitate's order. For example, in variant 1, slip system (111)[1 $\bar{1}$ 0] (n<sub>1</sub>l<sub>3</sub> in Figure. 2A) and slip system ( $\bar{1}\bar{1}$ 1) [ $\bar{1}$ 10] (n<sub>2</sub>l<sub>2</sub> in Figure. 2B) maintain the precipitate's order while the remaining ten slip systems disrupt the order. In this study, we refer the slip systems that maintain the ordering as type 1 configuration/interaction and slip system that cause disordering as type 2 configuration/interaction. From the geometric-based perspective, the corresponding twinning systems of type 2 slip systems are preferred to be active as the formation of the dislocation stacking fault maintains the precipitates' order. This explanation was used to rationalize the observation of deformation twinning in bulk scale mechanical tests [27,30,31].

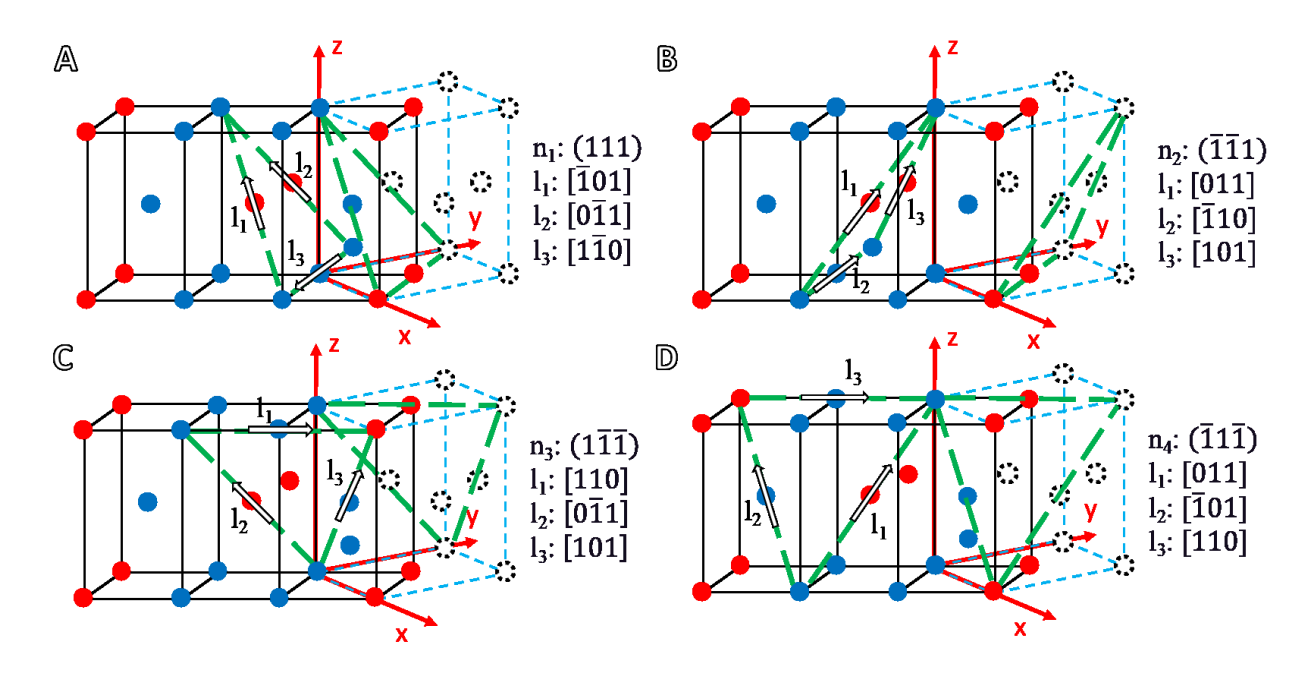


Figure 2. Crystalgraphic relationship between the 12 FCC slip systems and the  $Pt_2Mostructured$  precipitate for variant 1. The slip planes and the slip directions are represented as dashed green triangles and black-outlined white arrows, respectively. Slip systems with slip planes (111), ( $\overline{111}$ ), ( $\overline{111}$ ), ( $\overline{111}$ ) are shown in (A)-(D), respectively.

However, this explanation alone does not account for the observation of both slip and deformation twinning observed from bulk mechanical tests [64] when the existence of multiple OR variants are considered. From crystallographic analysis, it was found that each slip system cause disordering in the Pt<sub>2</sub>Mo-structured precipitate in five out of six OR variants. As an example, Figure 3 shows the crystallographic relationship between the slip system  $(1\bar{1}1)[\bar{1}01]$  and the six OR variants. In variant 4 (Figure 3D), the slip system  $(1\bar{1}1)[\bar{1}01]$  maintains the precipitate's order while it causes disordering in all other variants. Since it has been shown that multiple variants can coexist with homogenous distribution [62–64], type 2 configuration would always take place when the dislocations on any slip system interact with the Pt<sub>2</sub>Mo precipitate distribution. In other words, it would be always preferable for the twinning systems to be active over slip according to the geometric-based approach. Due to the occurence of slip in experiments, type 2 interaction does not always induce deformation twinning; and there must be other factors that influence that activation of different deformation modes in Ni-based alloys containing Pt<sub>2</sub>Mo-structured precipitates. In other FCC deformation twinning literature, grain

orientations and resolved-shear stresses on partial dislocations have been observed to influence deformation twinning in low/medium stacking-fault-energy FCC metals (e.g. Cu [65]) and FCC nanocrystalline metals [66]. To explore the different factors on the activation of slip versus twinning, our study first examines the influence of type 1 and type 2 interactions on stacking fault formation. Secondly, the grain orientation effect (i.e. effect of resolved shear stresses on dislocation partials) is considered for type 2 interaction. Lastly, the mechanism for deformation twinning induced by Pt<sub>2</sub>Mo-structured precipitates is proposed using molecular dynamics energy-based approach.

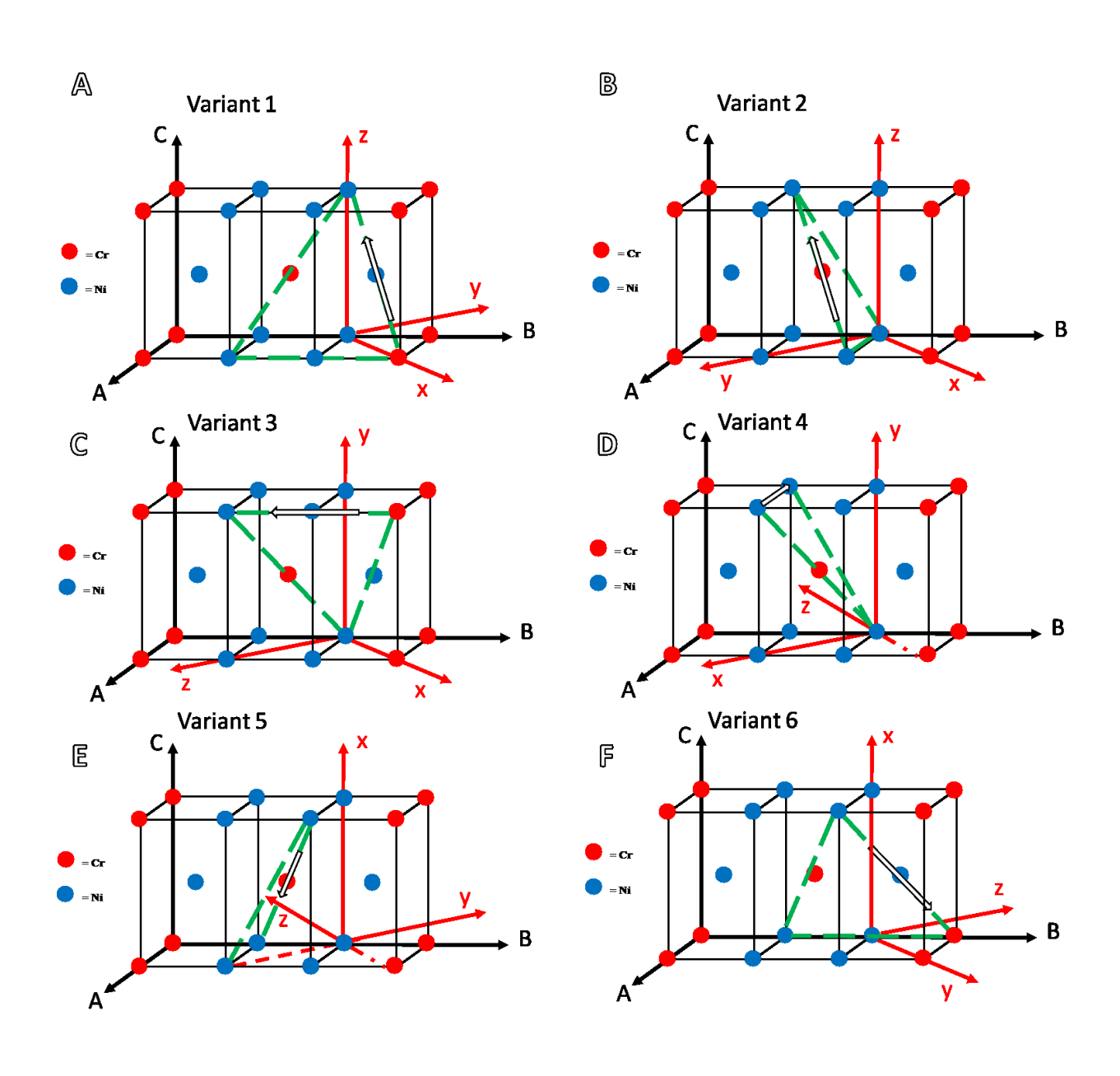


Figure 3. Schematic representations of  $(1\bar{1}1)[\bar{1}01]$  slip system for six variant orientation relationships of Ni<sub>2</sub>Cr-type, Pt<sub>2</sub>Mo-structure precipitate and FCC matrix. (A)-(F) correspond to variants 1-6, respectively. x-, y-, z-axes corresponding to the [100], [010], and [001] of the FCC Ni matrix. A-, B-, C-axes correspond to the Pt<sub>2</sub>Mo-structured orientations of each variant in Table 1.

#### 3. Methods

## 3.1. Materials preparation

A Ni<sub>2</sub>Cr binary alloy was produced by small batch arc-melting, followed by hot-rolling, and homogenized for 24 h at 1093 °C. One batch of the Ni<sub>2</sub>Cr alloy was aged inside the furnace at 475°C for 10,000 h. To accurately monitor the temperature, three thermocouples were placed around the samples and monitored throughout the aging process. The full detail of the material fabrication and aging process is reported in [67]. The aging process was performed to induce precipitation of Ni<sub>2</sub>Cr LRO precipitates.

## 3.2. Molecular dynamics simulations

Using LAMMPS [68], the molecular dynamics (MD) simulation work consists of two parts. The first part examines the interaction between a single dislocation and a Pt<sub>2</sub>Mostructured precipitate for the type 1 and type 2 interactions. In particular, the influence of type 2 interaction and the role of dislocation partials' resolved shear stresses on the formation of stacking fault are investigated. The angular-dependent potential (ADP) for Ni-Cr system developed by Howells and Mishin is utilized since it can capture the elastic constants, lattice spacing and defect energies (stacking fault energies) of both individual elements and binary alloys [69]. OVITO is used to visualize all of the MD results [70]. As shown in Figure. 4, a spherical LRO Ni<sub>2</sub>Cr precipitate is placed at the center of the simulation cell and surrounded by disordered FCC Ni<sub>2</sub>Cr matrix atoms. The LRO Ni<sub>2</sub>Cr precipitate is generated by rotating atoms within a defined spherical region to the Pt2Motype crystal structure according to the OR variant 2. The matrix atoms are randomly generated using the FCC lattice while maintaining the stoichiometry of 2:1 for Ni and Cr atoms. An edge dislocation dipole is introduced with use of the displacement field of a dislocation shear loop [71-73]. Since the initial displacement field does not describe properly the dislocation core structure, energy minimization via a nonlinear conjugate gradient method is performed to relax the core structure after inserting the dislocation. The system is then brought to thermodynamic equilibrium at 10 K using a Nose-Hoover style thermostat and barostat [74]. This dislocation is then driven towards the precipitate under different applied shear stresses.

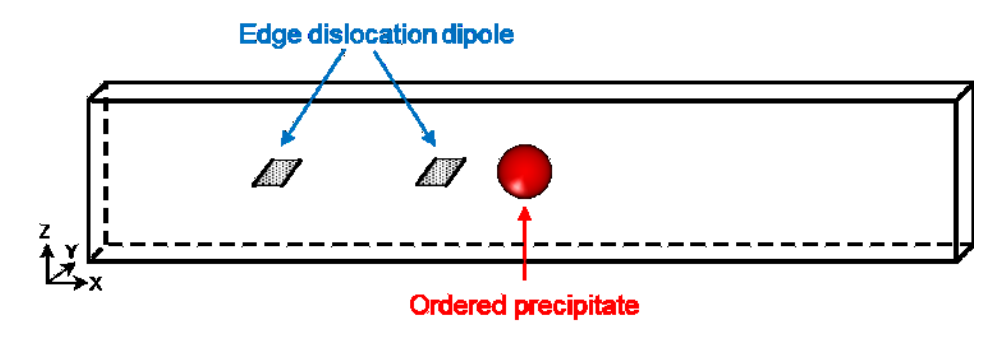


Figure 4. Simulation cell with an edge dislocation dipole and an ordered Ni<sub>2</sub>Cr precipitate The simulation cell is oriented such that the X, Y, and Z axis are in the <101>, <121>, and <111> directions, respectively. Periodic boundary conditions are used in all 3 directions. The simulation cell is approximately  $302.0 \times 12.2 \times 49.2 \,\mathrm{nm}^3$  in X, Y, and Z directions and contains about 16 million atoms. The X dimension is much longer than the other two dimensions to minimize the effects of the dislocation dipole self-interaction. Two different slip systems  $[110](\bar{1}1\bar{1})$  and  $[101](1\bar{1}1)$  are studied to understand the role of loading orientation on the interaction between dislocation and the LRO Ni<sub>2</sub>Cr precipitates. For the  $[110](\bar{1}1\bar{1})$  slip system, a 350 MPa pure shear stress is applied in the full Burgers' vector direction. Moreover, for the  $[101](1\bar{1}1)$  slip system, two different stress states are considered: (1) 750 MPa pure shear stress in the direction of the full dislocation (which results in a 650 MPa resolved shear stress on both dislocation partials ) and (2) 650 MPa pure shear stresses acting on the Shockley's partials on the outcome of the interaction.

To explore possible twin formation process, the second part of MD simulations focuses on the interactions between multiple coplanar dislocations with a  $Pt_2Mo$ -structured precipitate for type 2 interactions. Specifically, the interaction between three consecutive coplanar  $[101](1\overline{11})$  dislocations with the  $Pt_2Mo$ -structured precipitate under an applied shear stress of 350 MPa in the Burgers vector direction is investigated. To rationalize the observed mechanism, generalized SF energy (GSFE) curves of the  $Pt_2Mo$ -structured,

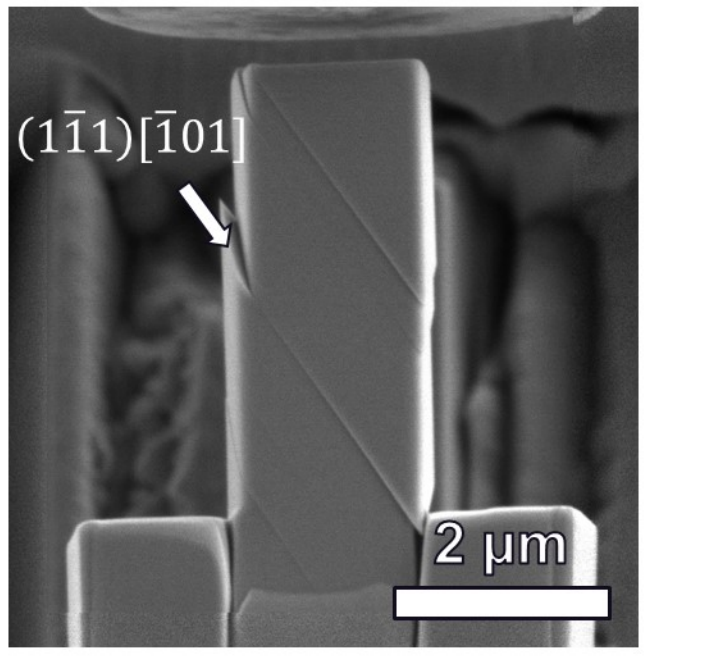
Ni<sub>2</sub>Cr-typed precipitate are investigated by shifting the top six layers along the  $\langle 12\overline{1}\rangle$  direction by the Burgers vector of the Shockley partial  $\frac{a}{6}\langle 12\overline{1}\rangle$ .

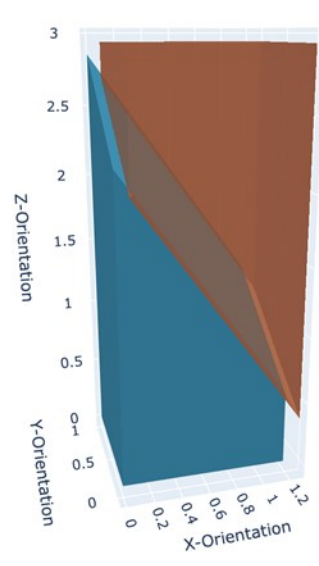
## 3.3. Experimental methods

As discussed in section 2, due to the existence of multiple OR variants, it is not possible to only have type 1 interaction during dislocation glide; and type 2 interaction is significantly more dominant compared to type 1 interaction during dislocation glide. Therefore, two sets of single-crystal micropilllars were fabricated and tested in two different loading orientations to study the role of grain orientations, as well as Schmid factors of partial dislocations, on activating different deformation modes for type 2 interaction. A FEI Quanta 3D dual-beam scanning electron microscope (SEM)/focused ion beam (FIB) was utilized for the fabrication of the micropillars and the observation of the subsequent testing. Electron backscatter diffraction (EBSD) was performed to map out the grain orientations; and the details of crystal orientations are shown in section 4.2. The micropillars were then fabricated with a square cross-section (~2 µm x ~2 µm) and side:length aspect ratios of 1:2.5-3. The bulk material removal was accomplished with a FIB beam of 2 nA at 30 keV and the final polishing was with a 0.3 nA beam at 16 keV. A detailed procedure is reported in [53]. The in situ microcompression tests were performed in the SEM using a Hysitron PI-88 Picoindenter. The tests were conducted at a strain rate of 2x10<sup>-3</sup>/s. Videos of the *in situ* tests were recorded for direct observation of the resulting deformation behavior of the micropillars during testing. The representative videos were shown in the Supplementary section.

A Python script was used to visualize the micropillars and the activated slip such as to perform slip trance analysis. The procedures are detailed as followed. A representative pillar volume is created with the sample dimensions and crystal orientation obtained from SEM images and EBSD, respectively. The locations of the activated slip are measured in the post-deformation SEM images, as shown in Figure 5A for instance. To visualize dislocation slip, at the locations of the slip events, the top half of the representative pillar volume is shifted with respect to the bottom half along the slip plane and the burger direction of each of the 12 slip systems in FCC, like in Figure 5B. The slip system that provides the best match as compared to the post-deformation SEM images is determined to be the active slip system. For example, Figure 5A presents the post-deformation SEM

image of a representative aged micropillar, showing dislocation slip. In the representative pillar volume in Figure 5B, the slip system  $(1\bar{1}1)[\bar{1}01]$  provides the best match to the activated slip in Figure 5A; therefore, slip system  $(1\bar{1}1)[\bar{1}01]$  is determined to be the active slip system. In case of deformation twinning, for a given loading direction, the leading partials and trailing partials can be determined for the different perfect Burger vectors using the Thompson Tetrahedron [75]. Similarly, the procedure can be applied to identify the active deformation twinning systems.





 $(1\bar{1}1)[\bar{1}01]$ 

Figure 5. (A) The SEM image of a deformed micropillar with Euler angles (141.6°, 35.5°, -142.9°). (B) The representative pillar volume of the tested micropillar shows that the activated slip system is determined to be  $(1\bar{1}1)[\bar{1}01]$ 

The post-deformation microstructure was characterized by TEM. TEM lamellae of several deformed micropillars were lifted out and prepared with the FIB. The microstructures presenting within the lamella were characterized using selected area electron diffraction (SAED), bright-field (BF), and dark-field (DF) TEM. An FEI Tecnai F30 and an image-corrected FEI Titan 80-300, both operated at accelerating voltage of 300 kV, were employed to record the deformed microstructures.

### 4. Results and analysis

In this section, the results and analysis are arranged as followed. Section 4.1 presents the first part of the MD results in which isolated interaction between an edge dislocation

with a Pt<sub>2</sub>Mo precipitate is examined. The influence of type 1 and type 2 as well as the role of resolved shear stresses on dislocation partials on the formation of stacking fault is examined. Section 4.2 then provides experimental evidence via micropillar compressions and TEM characterization to investigate the grain orientation effect (directly related to resolved shear stresses on dislocation partials) on the two deformation modes (slip versus twinning). To connect the experimental observation of deformation twinning with the stacking fault formation showed via MD (section 4.1) in type 2 interaction, section 4.3 presents the second part of the MD results examining the twin formation process from an intrinsic stacking fault (ISF) using an energy-based approach.

## 4.1. Isolated interaction between an edge dislocation with the Pt<sub>2</sub>Mo-structured precipitate via MD simulations

Four different configurations for the interaction between dislocation and the LRO Ni<sub>2</sub>Cr precipitate with OR variant 2 are shown in Figure 6. Specifically, Figure 6A shows the interaction between an  $[110](\bar{1}1\bar{1})$  (type 1 for OR variant 2) edge dislocation with the precipitate under 350 MPa pure shear stress in the [110] direction. Figures 6B and 6C show the interaction between an  $[101](1\overline{1}\overline{1})$  (type 2 interaction for all variants except OR variant 3) edge dislocation with the precipitate in the [101] direction under 350 and 750 MPa pure shear stress, respectively. In the last configuration, Figure 6D shows the type 2 interaction between an  $[101](1\overline{11})$  edge dislocation with the precipitate under a 650 MPa shear stress in the leading partial to explore the effects of applied shear stress on the Shockley's partials to the outcome of the reaction. For FCC systems, it is energetically favored for the perfect dislocation to dissociate into two Shockley partials connected by an intrinsic stacking fault [75,76]. The leading and trailing partials of the  $[110](\bar{1}1\bar{1})$  edge dislocation are  $[121](\bar{1}1\bar{1})$  and  $[21\bar{1}](\bar{1}1\bar{1})$ , respectively; and the leading and trailing patials of the  $[101](1\overline{11})$  edge dislocation are  $[211](1\overline{11})$  and  $[1\overline{12}](1\overline{11})$ , respectively. For slip systems with the [110] Burgers' vector (type 1) shown in Figure 6A, the dislocation easily glides through the precipitate since it does not cause the anti-phase boundary inside the precipitate. In fact, for other slip systems under the same 350 MPa applied shear stress, only the leading partial glides through the precipitate (as shown in Figure 6B for the [101] Burgers' vector). In these cases (i.e. type 2), the trailing partial is pinned by the precipitate due to the extra energy barrier caused by the APB which would form

when the trailing partial sweep through the precipitate. This indicates that the resolved shear stress of  $350\cos 30^{\circ} \approx 303$  MPa on the trailing partial is insufficient to push the trailing partial through the precipitate and create the APB in the process. When the shear stress is increased up to 750 MPa which results in a 650 MPa resolved shear stress on both partials, the trailing partial can glide through and disorder the Pt<sub>2</sub>Mo-structured precipitates, as shown in Figure 6C for the  $[101](1\overline{11})$  edge dislocation. Importantly, the resolved shear stress on the trailing partial is essential to the outcome of the interaction. This is shown in Figure 6D for the same slip system but under different stress state of 650 MPa shear stress in the leading partial, which is identical to the resolved shear stress on the leading partial of the configuration shown in Figure 6C. However, the resolved shear stress on the trailing partial is only  $650\cos 60^{\circ} \approx 325$  MPa, which is much lower than the resolved shear stress acting on the trailing partial of the configuration shown in Figure 6C (650 MPa). As a result, only the leading partial can glide through the precipitates while the trailing partial is pinned, which elongates the ISF between these partials. Consistent with the geometric-based explanation, configurations 1 and 2 (Figures 6A and 6B) show that the type 2 interaction elongate the stacking fault width as the APB formation energy prevents the trailing partial from easily gliding through the precipitate as compared to type 1 interaction. The elongation of intrinsic stacking fault is considered as the prerequisite for deformation twinning in FCC matrix; however, this phenomenon does not fully explain the deformation twinning. In part 2 of the MD work under section 4.4, an energy-based approach is used to demonstrate the twin formation process due to the Pt<sub>2</sub>Mo-structured precipitates. Additionally, configurations 1 and 2 show that type 2 interaction provide higher resistance to dislocation motion compared to type 1 interaction. Therefore, in the presence of multiple OR variants, the dislocation and precipitate interaction during dislocation glide is governed by type 2 interaction because type 2 is the most dominant and provide more resistance compared to type 1. Another important finding comes from the comparison between configurations 3 and 4 (Figures 6C and 6D) showing that the resolved shear stresses acting on the dislocation partials significantly influence the stacking fault width during dislocation-precipitate interaction. This finding suggests that type 2 interaction does not necessarily lead to deformation twinning as the role of the resolved shear stresses on the partial dislocations need to be considered. In

other words, the grain orientations are expected to influence the outcome of the deformation modes (slip versus twinning) because they directly vary the resolved shear stresses acting on the dislocation partials. To prove this MD observation, micropillar compressions of single crystal Ni<sub>2</sub>Cr are tested in two specific loading orientations with different Schmid factors of the dislocation partials.

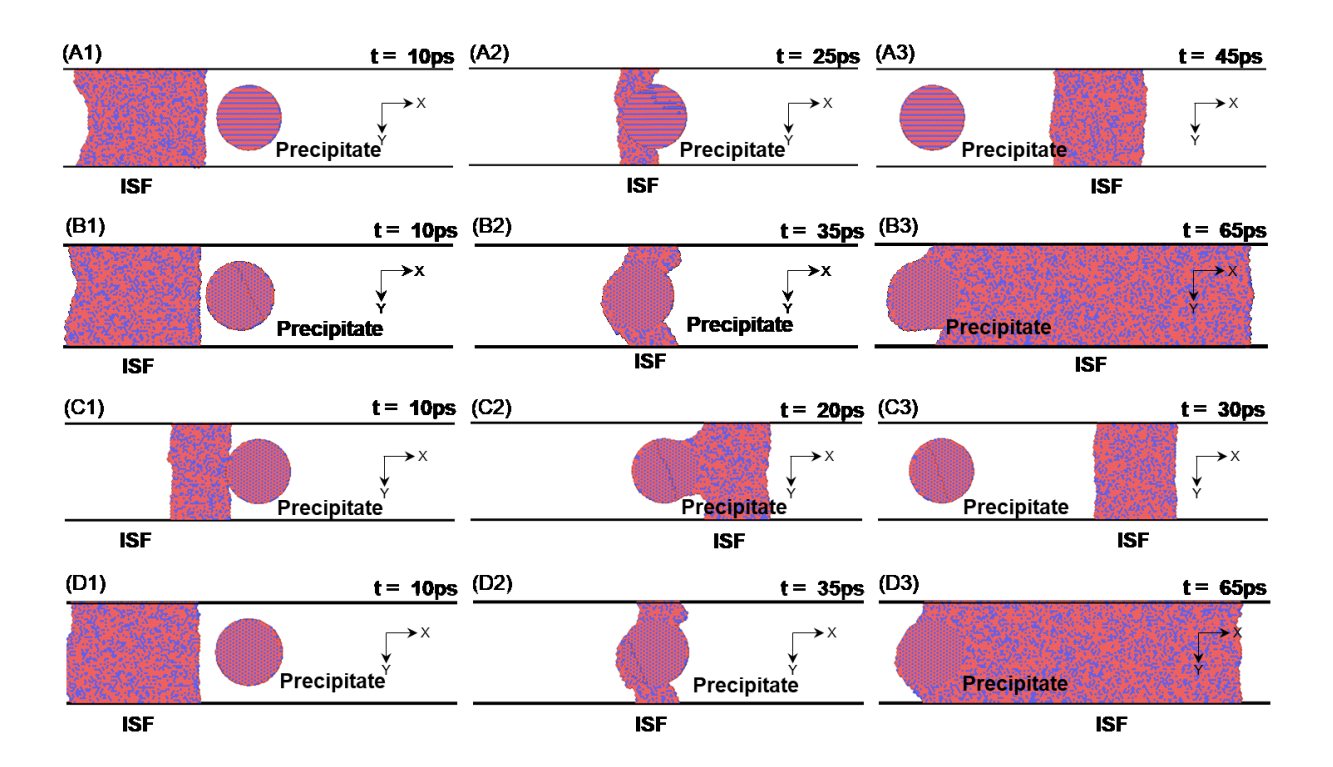


Figure 6. Top view of dislocation – precipitate interactions. (A1), (A2), and (A3) are snapshots of  $[110](\bar{1}1\bar{1})$  edge dislocation (type 1) interaction with precipitate under 350 MPa pure shear stress in the Burgers' vector direction at 10, 25, and 45 ps, respectively. (B1), (B2), and (B3) are snapshots of  $[101](1\bar{1}\bar{1})$  (type 2) edge dislocation interaction with precipitate under 350 MPa pure shear stress in the Burgers' vector direction at 10, 35, and 65 ps, respectively. (C1), (C2), and (C3) are snapshots of  $[101](1\bar{1}\bar{1})$  (type 2) edge dislocation interaction with precipitate under 750 MPa pure shear stress in the Burgers' vector direction at 10, 20, and 30 ps, respectively. (D1), (D2), and (D3) are snapshots of  $[101](1\bar{1}\bar{1})$  (type 2) edge dislocation interaction with precipitate under 650 MPa pure shear stress in the leading Shockley's partial at 10, 35, and 65 ps, respectively.

#### 4.2. Micropillar compression

Two sets of micropillars were tested. Set 1 has the Euler angles of (141.6°, 35.5°, -142.9°) and set 2 has the Euler angles of (-78.6°, 70.9°, -69.9°). Three micropillars of each set

were tested to failure and the resolved shear stress versus strain plots of those tests are shown in Supplementary Figure 1. Additional tests were performed and stopped slightly pass yielding for TEM characterization of the deformed pillars. The representative resolved shear stress versus strain plots of the two sets are shown in Figure 7A. The set 1 micropillars deformed only via dislocation slip (Figure 7B) while the set 2 micropillars deformed via deformation twinning followed dislocation slip (Figure 7C). The representative test videos of sets 1 and 2 are Supplementary Videos 1 and 2, respectively. In both sets, the slip events are highly localized and corresponded to intense strain bursts while the twin events show stabilized plastic flow, as indicated in Figure 7A. Supplementary Figure 2 presents another example of a set 2 micropillar compressed to failure, in which intense strain localization and failure occurred along a single localized slip. The average critical resolved shear stress values (CRSS) of deformation twinning and slip, calculated by multiplying the Schmid factors of active slip or twin systems and the measured yield stress values, are 166 ± 13 MPa and 247 ± 33 MPa, respectively.

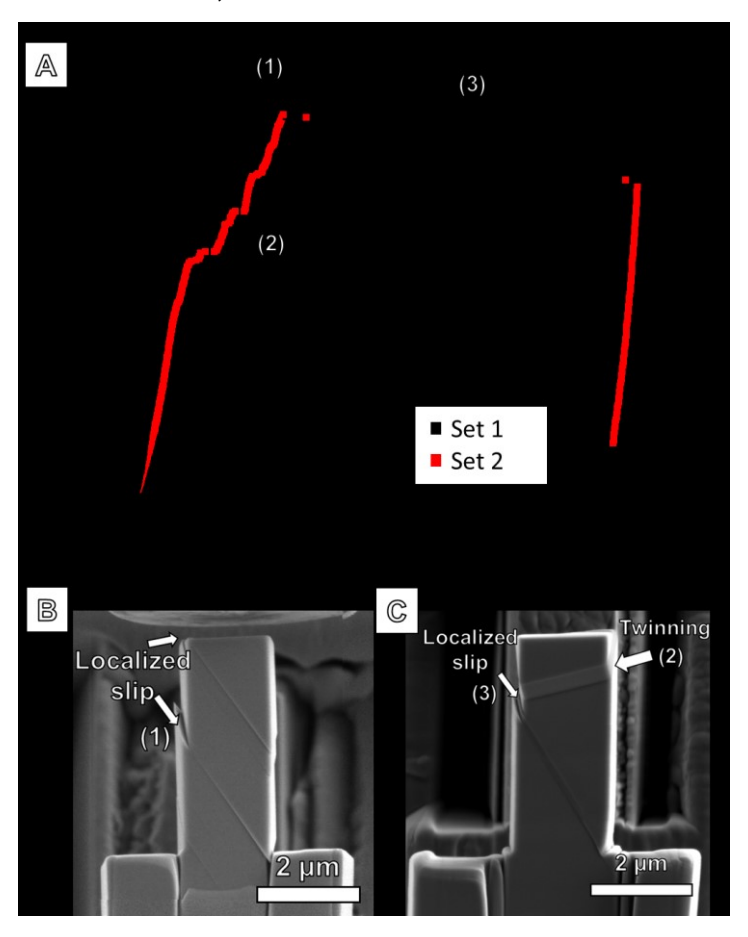


Figure 7. (A) The representative resolved shear stress-strain curves of sets 1 and 2. The SEM images of (A) a representative deformed micropillar set 1, (B) a representative deformed micropillar set 2. The different deformation events are indicated with arrow signs and correlated with the stress-strain curves

To determine the active slip/twin systems, slip trace analysis was performed in both sets. In set 1, the activated slip system is determined to be  $(1\bar{1}1)[\bar{1}01]$  as shown in Figure 5. Table 2 shows the Schmid factor of the perfect dislocation (SF<sub>P</sub>), leading partial (SF<sub>LP</sub>), and trailing partial (SF<sub>TP</sub>) for all slip systems for set 1. The activated slip system  $(1\bar{1}1)[\bar{1}01]$  has the highest SF<sub>P</sub>, SF<sub>LP</sub>, and SF<sub>TP</sub>. The SF<sub>LP</sub> (0.311) is lower than the SF<sub>TP</sub> (0.432); thus, the resolved shear stress along the trailing partial is ~1.4 (0.432/0.311) times higher than that of the leading partial. Slip was found to take place over deformation twinning. The higher resolved shear stress on the trailing partial means a higher driving force for the trailing partial to overcome the ordered precipitate and close the intrinsic stacking fault; therefore, it is consistent with the observation found by the MD results in section 4.1.

Table 2. The Schmid factors for the leading partials ( $SF_{LP}$ ), trailing partials ( $SF_{TP}$ ), and the perfect Burger vectors ( $SF_{PD}$ ) for micropillar set 1's slip systems. The loading direction is [-0.350, -0.463, 0.814] and the pillars' Euler angles are (141.6°, 35.5°, -142.9°). The activated slip system is bolded.

Slip systems	Leading partial	Trailing partial	SFPD	SFLP	SFTP
$(111)[1\bar{1}0]$	$(111)[2\overline{1}\overline{1}]$	$(111)[1\bar{2}1]$	0.000	0.000	0.000
$(111)[\bar{1}01]$	$(111)[\overline{1}\overline{1}2]$	$(111)[\bar{2}11]$	0.000	0.001	0.000
$(111)[01\overline{1}]$	$(111)[\bar{1}2\bar{1}]$	$(111)[11\bar{2}]$	0.000	0.000	0.001
$(11\overline{1})[1\overline{1}0]$	$(11\bar{1})[2\bar{1}1]$	$(11\overline{1})[1\overline{2}\overline{1}]$	0.075	0.221	0.091
$(11\overline{1})[\overline{1}0\overline{1}]$	$(11\overline{1})[\overline{2}1\overline{1}]$	$(11\overline{1})[\overline{1}\overline{1}\overline{2}]$	0.308	0.221	0.313
$(11\overline{1})[0\overline{1}\overline{1}]$	$(11\bar{1})[1\bar{2}\bar{1}]$	$(11\overline{1})[\overline{1}\overline{1}\overline{2}]$	0.233	0.091	0.313
$(1\bar{1}1)[110]$	$(1\bar{1}1)[121]$	$(1\bar{1}1)[21\bar{1}]$	0.308	0.101	0.432
$(1\overline{1}1)[10\overline{1}]$	$(1\bar{1}1)[1\bar{1}\bar{2}]$	$(1\overline{1}1)[21\overline{1}]$	0.441	0.331	0.432
$(1\overline{1}1)[0\overline{1}\overline{1}]$	$(1\bar{1}1)[1\bar{1}\bar{2}]$	$(1\overline{1}1)[\overline{1}\overline{2}\overline{1}]$	0.133	0.331	0.101
$(\bar{1}11)[110]$	$(\bar{1}11)[211]$	$(\overline{1}11)[12\overline{1}]$	0.233	0.058	0.346
$(\overline{1}11)[\overline{1}0\overline{1}]$	$(\bar{1}11)[\bar{1}1\bar{2}]$	$(\overline{1}11)[\overline{2}\overline{1}\overline{1}]$	0.133	0.288	0.058
$(\overline{1}11)[01\overline{1}]$	$(\overline{1}11)[\overline{1}1\overline{2}]$	$(\overline{1}11)[12\overline{1}]$	0.366	0.288	0.346

Figure 8A and 8B show the two deformation behaviors observed in set 2 where deformation twinning on slip system  $(\bar{1}11)[211]$  followed by slip either on  $(1\bar{1}1)[\bar{1}01]$  slip system (Figure 8A) or on  $(11\bar{1})[\bar{1}11]$  slip system (Figure 8B). Figure 8C,8D, and 8E show the slip system visualization for all the observed active slip systems.

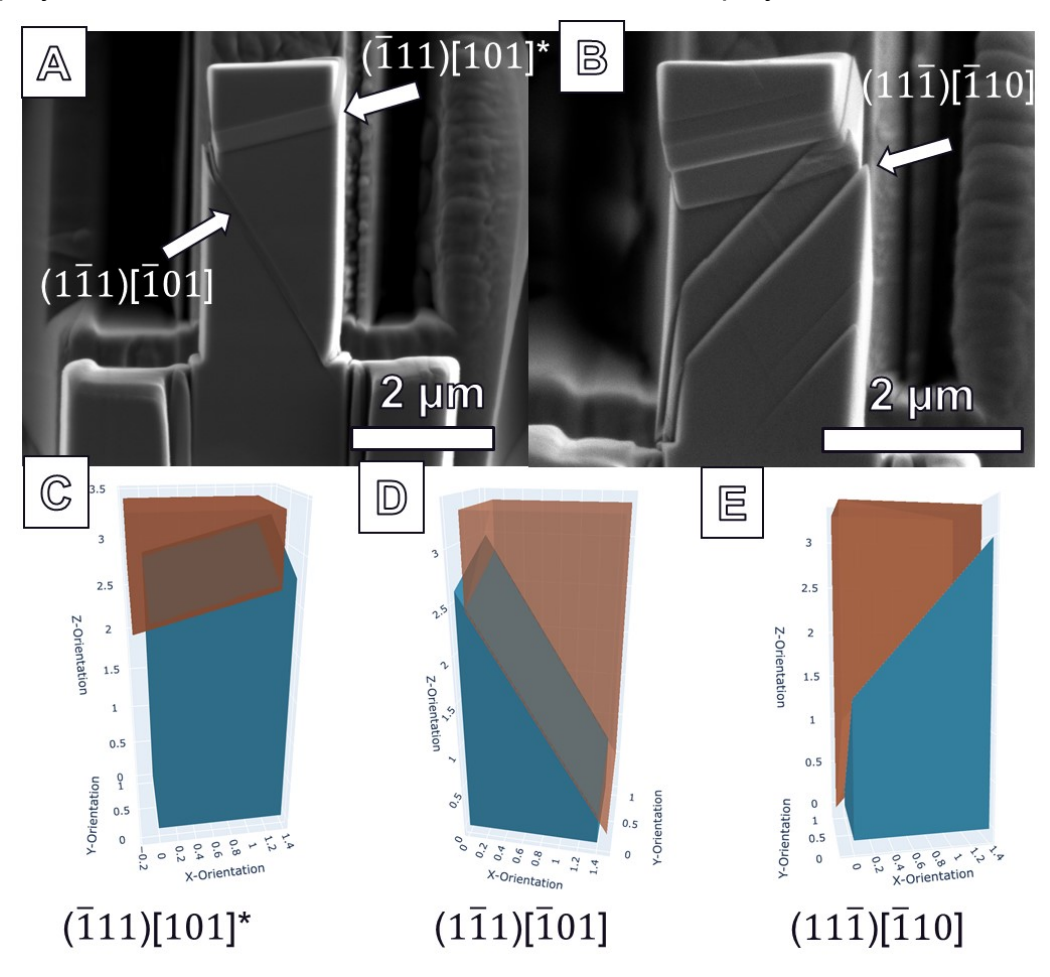


Figure 8. (A)(B) show the SEM images of two representative deformed micropillars with Euler angles (-78.6°, 70.9°, -69.9°). Using the visualization script, the simulated slip systems (C)  $(\bar{1}11)[101]$ , (D)  $(1\bar{1}1)[\bar{1}01]$ , and (E)  $(11\bar{1})[\bar{1}10]$  were shown by displacing the corresponding slip planes of the simulated micropillar along the Burger vector direction. \*Important to note, the leading partial of the slip system  $(\bar{1}11)[101]$  (C) is responsible for the deformation twinning observed in (A,B).

Similarly, in Table 3, SF<sub>PD</sub>, SF<sub>LP</sub>, and SF<sub>TP</sub> values are reported for all slip systems. Although slip system ( $\bar{1}11$ )[ 101] does not have the highest SF<sub>P</sub> (0.352) compared to the secondary activated slip systems ( $11\bar{1}$ )[  $\bar{1}10$ ] (0.440) and ( $1\bar{1}1$ )[  $\bar{1}01$ ] (0.439), the

corresponding leading partial of slip system ( $\bar{1}11$ )[ 101] has the highest SF<sub>LP</sub> (0.408) out of all slip systems and slightly higher than the secondly activated slips' SF<sub>LP</sub>. Secondly, the trailing partial of the slip system ( $\bar{1}11$ )[ 101] has a very low SF<sub>TP</sub> compared to the secondary activated slip systems' SF<sub>TP</sub> (0.372 and 0.371). Another point is that the Schmid factors of the leading and trailing partials are very similar in the slip case in contrast to the twin case, where the Schmid factor of the leading partial is significantly higher than that of the trailing partial. The deformation response from both sets indicates that the activation of deformation twinning from type 2 interaction depends on the Schmid factors of the dislocation partials (i.e. grain orientations). Deformation twinning takes place when the driving force on the leading partial is higher than that of the trailing partial; and, slip takes place when the driving force on the leading partial is similar or lower than that of the trailing partial. Therefore, grain orientations play major role in the activation of deformation twinning versus slip in Ni-based alloys containing Pt<sub>2</sub>Mo-structured precipitates, confirming the MD results.

Table 3. The Schmid factors for the leading partials ( $SF_{LP}$ ), trailing partials ( $SF_{TP}$ ), and the perfect Burger vectors ( $SF_{PD}$ ) for micropillar set 2's slip systems. The loading direction is [-0.888, 0.325, 0.327] and the pillars' Euler angles are (-78.6°, 70.9°, -69.9°). The slip systems activated are bolded.

Slip Systems	Leading partial	Trailing partial	SF <sub>PD</sub>	SF <sub>LP</sub>	SFTP
$(111)[1\overline{1}0]$	$(111)[2\bar{1}\bar{1}]$	$(111)[1\bar{2}1]$	0.117	0.135	0.067
$(111)[\overline{1}01]$	$(111)[\bar{1}\bar{1}2]$	$(111)[\bar{2}11]$	0.117	0.068	0.135
$(111)[01\bar{1}]$	$(111)[\overline{1}2\overline{1}]$	$(111)[11\overline{2}]$	0.000	0.067	0.068
$(11\mathbf{\overline{1}})[1\mathbf{\overline{1}0}]$	$(11\overline{1})[1\overline{2}\overline{1}]$	$(11\overline{1})[2\overline{1}1]$	0.440	0.391	0.372
$(11\overline{1})[101]$	$(11\bar{1})[112]$	$(11\bar{1})[2\bar{1}1]$	0.204	0.019	0.372
$(11\overline{1})[011]$	$(11\overline{1})[1\overline{2}\overline{1}]$	$(11\overline{1})[\overline{1}\overline{1}\overline{2}]$	0.237	0.391	0.019
$(1\overline{1}1)[110]$	(111)[121]	$(1\overline{1}1)[21\overline{1}]$	0.204	0.019	0.371
$(1\overline{1}1)[10\overline{1}]$	$(1\bar{1}1)[1\bar{1}\bar{2}]$	$(1\bar{1}1)[21\bar{1}]$	0.439	0.390	0.371
$(1\overline{1}1)[0\overline{1}\overline{1}]$	$(1\bar{1}1)[1\bar{1}\bar{2}]$	$(1\bar{1}1)[\bar{1}\bar{2}\bar{1}]$	0.236	0.390	0.019
$(\bar{1}11)[110]$	$(\bar{1}11)[211]$	$(\overline{1}11)[12\overline{1}]$	0.354	0.408	0.205
$(\overline{1}11)[101]$	$(\bar{1}11)[211]$	$(\overline{1}11)[1\overline{1}2]$	0.352	0.408	0.203
(111)[011]	$(\bar{1}11)[\bar{1}1\bar{2}]$	$(\bar{1}11)[12\bar{1}]$	0.001	0.203	0.205

## 4.3. Transmission electron microscopy analysis

To confirm the presence of the deformation twin in set 2, HR-TEM was performed on the deformed twinned micropillars. Figure 9A shows the HR-TEM image of the twinned micropillars with the sample oriented along the  $[01\overline{1}]$  axis, clearly shows the twin-matrix interface along  $(1\overline{1}\overline{1})$  plane. As shown in Figure 9B, the inset selected area electron diffraction (SAED) pattern shows the diffraction spots from both the matrix and the twin domains, confirming the presence of the deformation twin. {211} steps were observed along the twin-matrix interface; these steps are commonly observed in FCC metals [77]. The darkfield TEM (DF-TEM) images of the twin spot g1 and the matrix spot g2 (Figure 9B) are shown in Figures 9C and 9D, respectively. The resolved shear stress direction is indicated in the two DF-TEM images. The captured untwinned region, i.e. the matrixoriented domain in the middle of the twin, could mean that the leading partials can be pinned at locally precipitate-dense regions. Notably, the deformation twin continues passed the unpinned region. A hypothesis for twin deformation process is that as the trailing partial remained pinned by the ordered precipitates, the lead partial creates a fault as it shears the precipitates. After the first layer fault is formed, successive faults followed via the same process, leading to the formation and propagation of the twin domain. The twin formation process is investigated in the next section via MD.

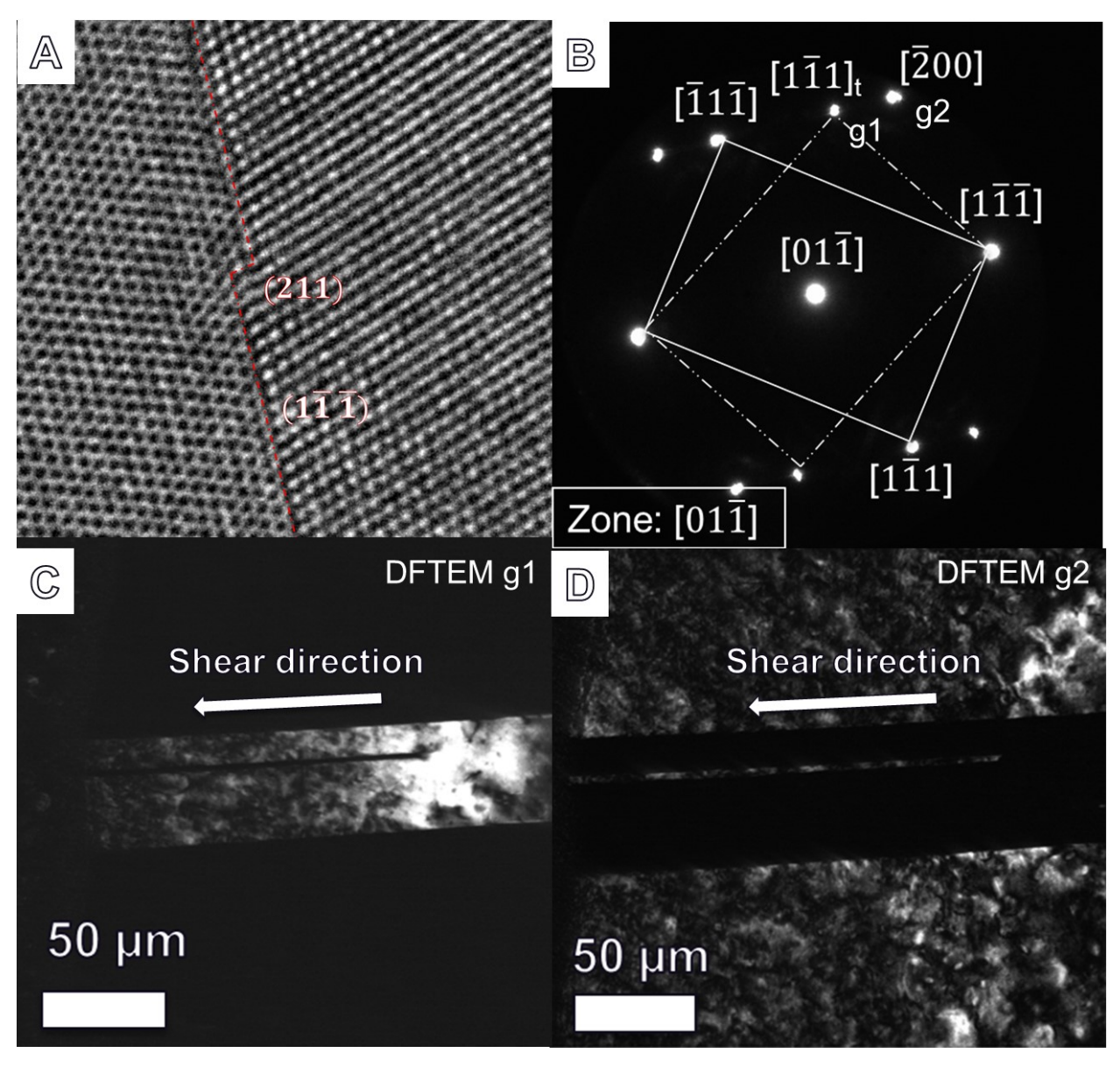


Figure 9. (A) HR-TEM micrograph of the twin/matrix interface. (B) the corresponding selected area electron diffraction (SAED) pattern oriented along the  $[01\overline{1}]$  zone axis. (C) The DF-TEM of the twin diffraction spot g1. (D) The DFTEM of the matrix diffraction spot g2

The precipitates' superlattice reflections can be seen in SAED pattern oriented along the <100> zone axis, shown in Figure 10A. The SAED pattern confirms the presence of the existence of OR variants 1 and 2 in the matrix for the Ni<sub>2</sub>Cr alloy in this study. The corresponding DF-TEM images of some selected precipitates spots are shown in Figures 10B-D. As a side observation, precipitates in the twin are not observed when imaging with diffraction spot g2, corresponding to OR variant 2 in the matrix (Figure 10C). However,

precipitates in the twin are observed with diffraction vectors g1 and g3, indicating at least one type of precipitate is present. Previous work on this material has confirmed the presence of three OR variants by recording SEAD pattern along the  $[\bar{1}12]$  zone axis [67]. M. Sundararaman et. al. [62] has indicated that the presence of OR variants 3-6 can be confirmed by recording SAED patterns along the [013] and  $[\bar{1}03]$ . Although we have not confirmed the existence of all six OR variants, the presence of at least three OR variants in our material still validates our observation of the dominant roles of type 2 interaction and grain orientations.

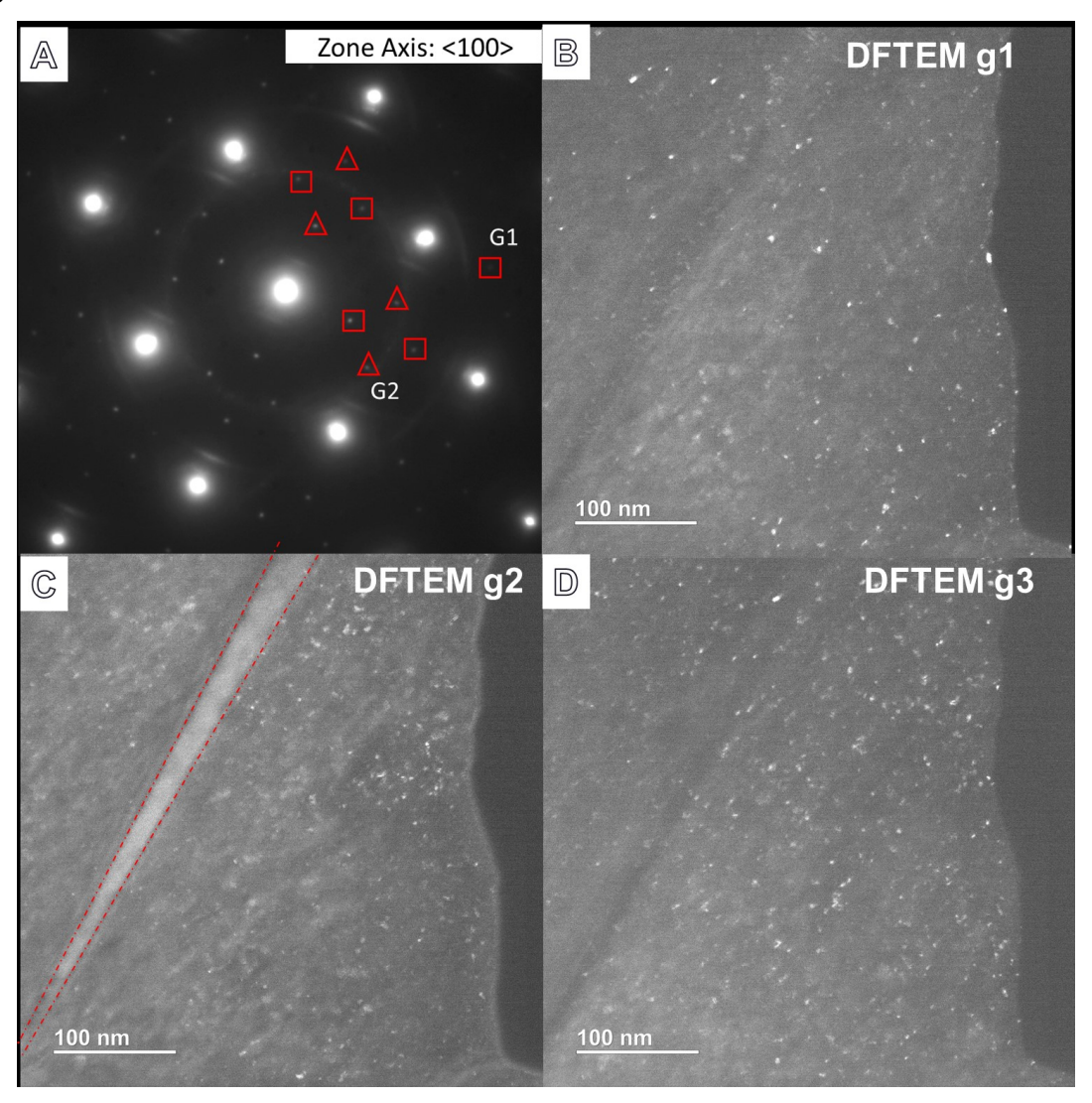


Figure 10. (A) The selected area electron diffraction (SAED) pattern oriented along the <100> zone axis, confirming the presence of multiple OR variants. OR variants 1 and 2 are indicated by the square and triangle symbols, respectively. (B),(C),(D) DF-TEM images of different respective precipitate diffraction spots g1-g3. The red dotted lines in (C) marks the boundaries of the twin domain.

## 4.4. Twin formation process from an ISF induced by type 2 interaction via MD simulations

So far, our MD results only show how type 2 interaction can lead to the formation of ISF. To rationalize with the experimental observation and confirm that the Pt<sub>2</sub>Mo-structured precipitates indeed lead to twinning, MD simulations were performed to demonstrate the twin formation process from a 1-layer twin (ISF) induced by type 2 interaction. While it is commonly agreed that twinning in FCC systems starts with the formation of ISF (sometimes called 1-layer twin), there are many proposed mechanisms for how the ISF evolves into a multiple-layer twin [78,79]. S. Mahajan has extensively outlined the different theories for twinning thickening process in FCC metals [78]. However, it has remained a challenge to provide direct experimental observations and detailed molecular dynamics work to confirm the proposed theories. Here, we applied MD simulations to propose a potential ISF-to-twin formation mechanism to explain the role of Pt<sub>2</sub>Mo-structured precipitates on deformation twinning.

One possible scenario is that the glide and interactions of multiple coplanar dislocations with the precipitate plays a role in triggering twinning. To model this scenario and assess this hypothesis, at the end of the configuration shown in Figure 6B, two more dislocations are inserted and driven toward the precipitates for interactions. Indeed, Figure 11 shows the interaction between multiple coplanar  $[101](1\overline{11})$  dislocations with the LRO precipitate under an applied shear stress of 350 MPa in the Burgers vector direction. This reaction is likely since multiple dislocations can be emitted from the same dislocation source from the free surface. The interaction of the 1st dislocation results in the passing of the leading partial and pinning of the trailing partials by the ordered precipitate. Figure. 11A, 11B, and 11C show the interaction of the 2<sup>nd</sup> dislocation with the ordered precipitate and Figure 11D and 11E show the interaction of the 3rd dislocation with the ordered precipitate. Figure 11F shows the intrinsic stacking fault formed by the leading partial of the 1<sup>st</sup> dislocation. Interestingly, when the 2<sup>nd</sup> dislocation arrives near the precipitate, there is a repulsive force between the leading partial of the 2<sup>nd</sup> dislocation and the trailing partial of the 1st dislocation. This provides an extra driving force for the trailing partial of the 1st dislocation to move out of the precipitate and generate the APB within the

precipitate in the process. The interaction of the 2<sup>nd</sup> dislocations' leading partial with the APB results in a 2-layer SF (i.e. an extrinsic stacking fault) inside the precipitate as seen in Figures. 11G and 11H. This newly formed 2-layer SF then acts as a barrier when the 3<sup>rd</sup> dislocation interacts with the precipitate. While there is also a repulsive force between the leading partial of the 3<sup>rd</sup> dislocation and the trailing partial of the 2<sup>nd</sup> dislocation, the pinning effects of the 2-layer SF inside the precipitate is significant and prevent the trailing partial of the 2<sup>nd</sup> dislocation to sweep through the precipitate. As a result, the leading partial of the 3<sup>rd</sup> dislocation cross-glide and forms the 2-layer SF in the matrix shown in Figures 11I and 11J. This process is repeated for the subsequent dislocations and thickening the twin in the process.

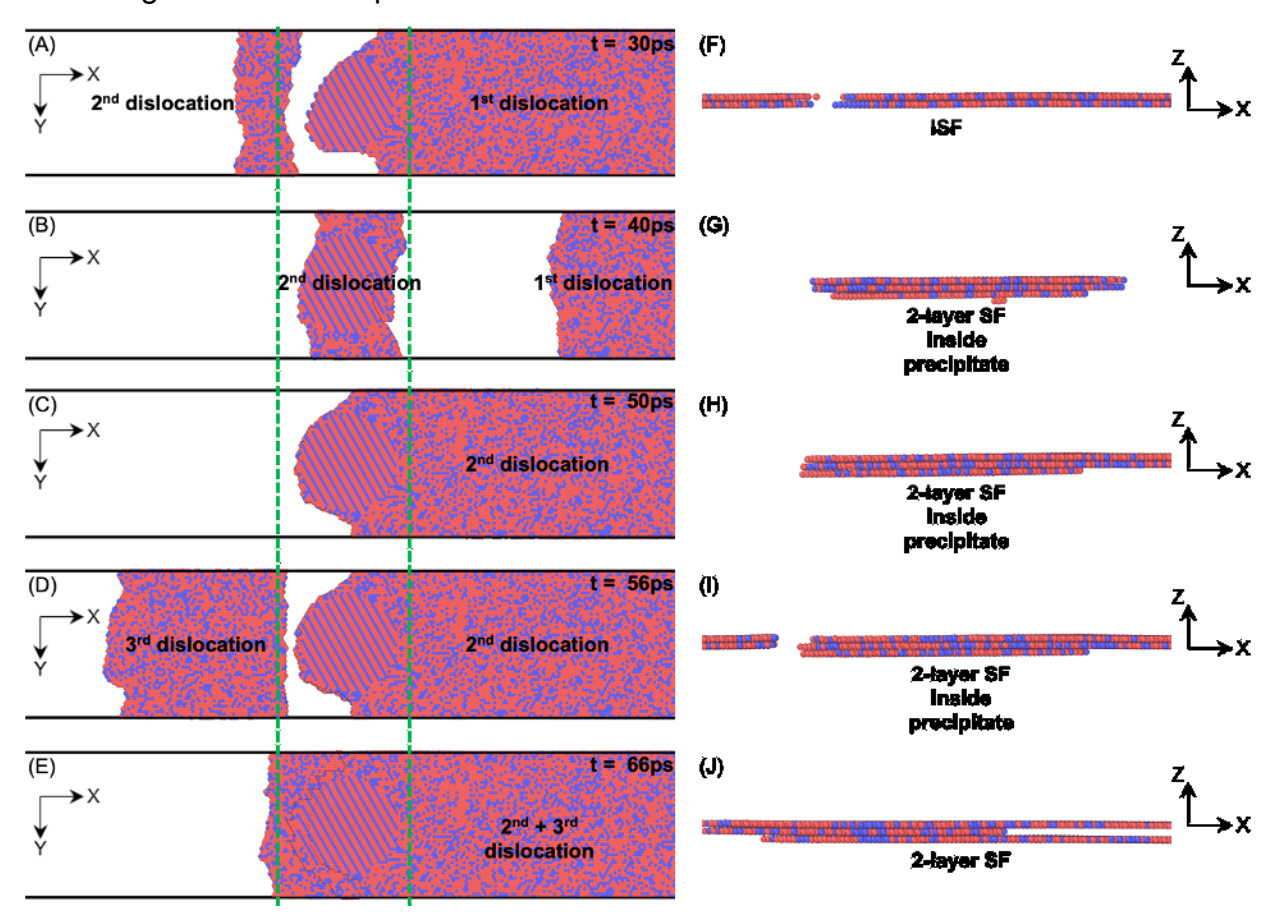


Figure 11. Top view of 3 co-planar edge dislocation – precipitate interactions at (A) 30 ps, (B) 40 ps, (C) 50 ps, (D) 56 ps, and (E) 66 ps. (F), (G), (H), (I), and (J) are the side view of the regions between two green dashed lines in (A), (B), (C), (D), and (E), respectively. Red atoms are Ni, while blue atoms are Cr. Perfect atoms are removed in all figures.

These MD results also indicate that the structures of the precipitate when the 1st and 2nd dislocations arrive are significantly different due to the formation of the APB after the trailing dislocation of the 1st dislocation sweeps through. However, these simulations do not rationalize why the interaction of the APB with the leading partial of the 2<sup>nd</sup> dislocation results in the 2-layer SF shown in Figures 11B and 11F. To further understand this process, generalized SF energy (GSFE) curves of the initial precipitate ordered structure and the one with APB are investigated. Figure 12 shows that the intrinsic SF energy of the precipitate is 62.8 mJ/m<sup>2</sup>. However, once the 1st dislocation passes through and creates an APB, the intrinsic SF energy of two consecutive  $(1\overline{1}\overline{1})$  atomic planes (the APB and the layer right below) is -227 mJ/m<sup>2</sup> as shown in Figure 9C. These negative SF energies indicate that the FCC structure will destabilize to become the HCP structure. Therefore, it is energetically favored for the atoms to be in HCP stacking inside the precipitate with the antiphase boundary. As a result, 2-layer SF is formed as shown in Figures 11G, and 11H. Similar behaviors of negative SF energies and nano-twin formation have been observed in FCC high entropy alloys [80]. Therefore, from an energy-based approach, MD results have shown that type 2 interaction can lead to deformation twinning, which is consistent with the experimental observations.

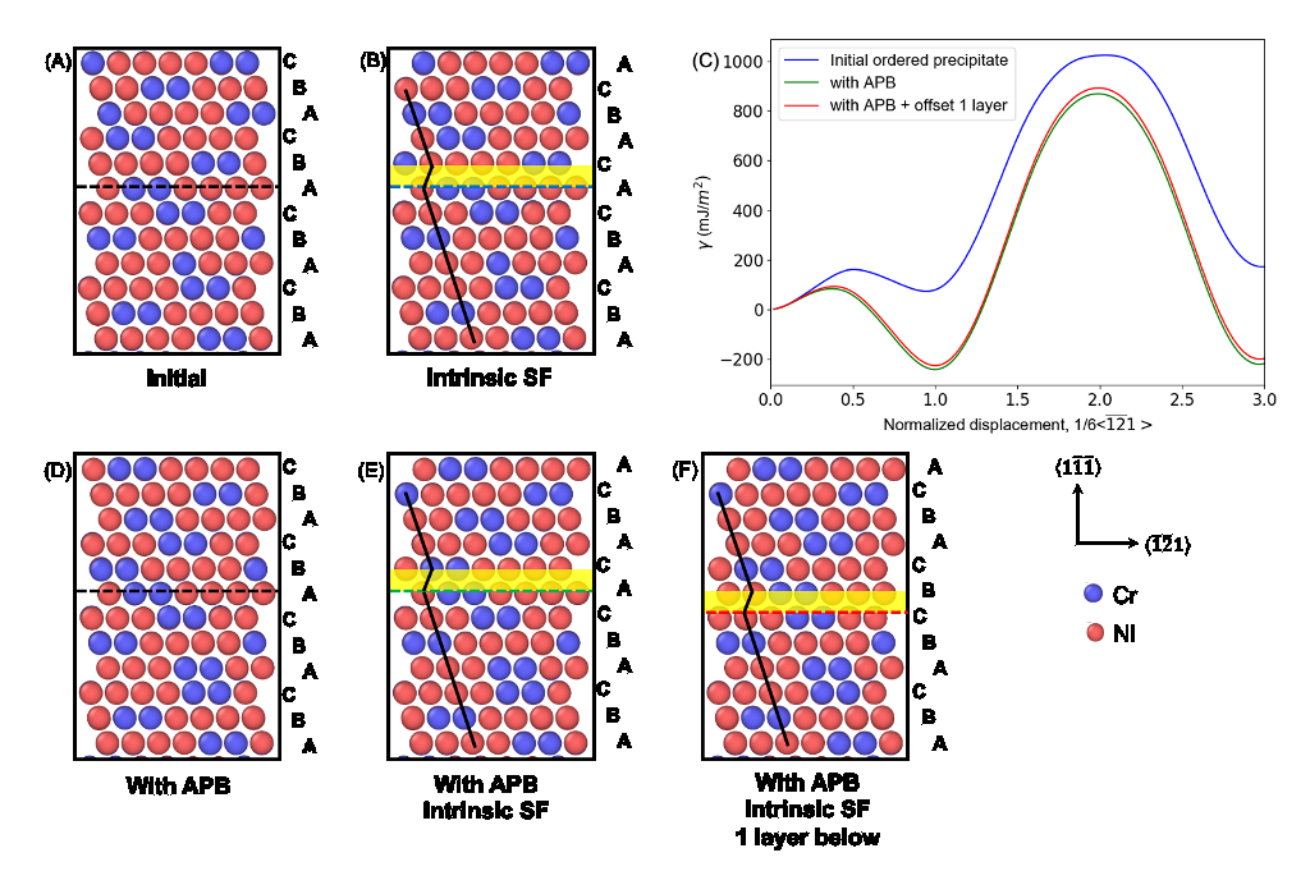


Figure 12. Atomic configurations of the original precipitate (A) initially and (B) with intrinsic SF. (C) Generalized SF energy (GSFE) curves of the perfect crystal structure and the antiphase boundary. Atomic configurations of the precipitate (D) with APB, (E) with APB and intrinsic SF, and (F) with APB and intrinsic SF of the layer below the APB. All configurations are viewed along the Burgers vector direction of the FCC matrix. Red atoms are Ni, while blue atoms are Cr. APB is marked by the black dashed lines.

## 4.5. Summary of the deformation twinning process

The schematic in Figure 13 summarizes the proposed deformation twinning process in Type 2 configuration. When the first dislocation interacts with the Pt<sub>2</sub>Mo-structured precipitates, the leading partial passes through the precipitates while the trailing partial is pinned. The stacking fault elongates as the leading partial continues to propagate (Figure 13A.) The addition of the APB term allows for sufficient interaction time for the second coplanar dislocation to interact with the trailing partial of the first dislocation. The leading partial of the second dislocation adds an additional forward force to unpin the first dislocation's trailing partial, leaving an APB behind (Figure 13B.) The leading partial interacts with the APB and forms an extrinsic fault (Figure 13C.). MD shows that such

process is energetically favorable. The second dislocation's leading partial continues to propagate. As the third dislocation approaches the 2-layer SF, the dislocation cross-glide and the leading partial propagates and forms the 2-layer SF in the matrix (Figure 13D.) We propose that the twin would thicken successively from the 2-layer SF by the repeating the process.

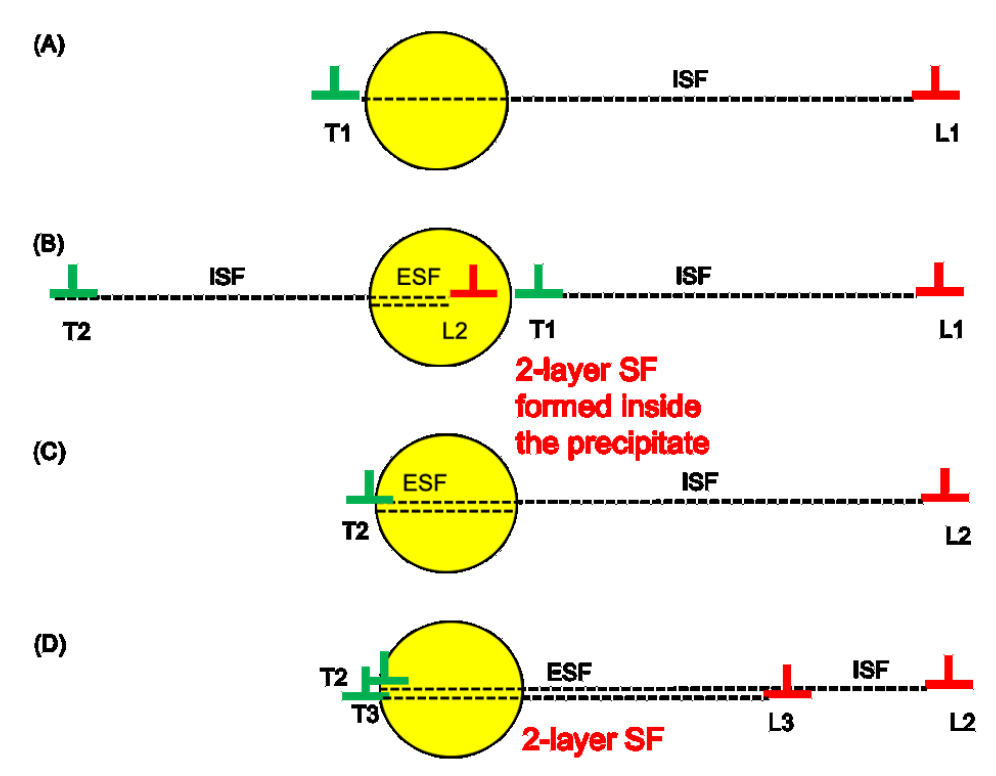


Figure 13. Schematic summarizing the MD observation of the formation of 2-layer fault from single-layer intrinsic fault.

#### 5. Discussion

## 5.1. Influence of the applied stress on partial dislocations and APB formation on stacking fault formation

As shown in the previous sections, the deformation mode depends on the interaction between the partials and the ordered precipitates. To qualitatively understand the different factors influencing the deformation mode, we look at the forces acting on the leading and trailing partials when they meet the precipitates. Figure 14 shows the partial dislocations and precipitate setup considered in our formulation. The different angles are defined in Figure 14. For simplicity, we consider the edge dislocations to be consistent with the MD simulation.

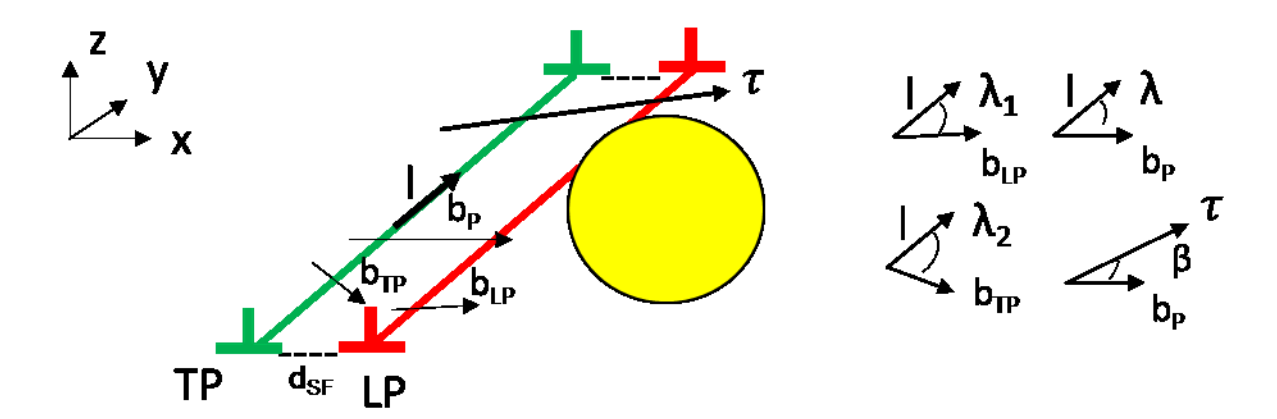


Figure 14. A schematic of the partial dislocations and precipitate arrangement; LP: leading partial, TP: trailing partial,  $d_{SF}$ : stacking fault width,  $b_p$ : perfect Burger vector,  $b_{LP}$ : leading partial's Burger vector,  $b_{TP}$ : trailing partial's Burger vector, I: line direction,  $\tau$ : applied shear stress,  $\lambda_1$ : the angle between the line direction and the leading partial's Burger vector,  $\lambda_2$ : the angle between the line direction and the trailing partial's Burger vector,  $\lambda$ : the angle between the line direction and the perfect Burger vector,  $\beta$ : the angle between the applied stress and the perfect Burger vector

Similar to the formulations proposed in [81], the equilibrium force equations of the leading and trailing partials are then written, for type 1 configuration, as:

$$\begin{split} F_{LP} &= b_p \tau cos(30^o - \beta) - \gamma_{SF} + \frac{Gb_P^2}{2\pi d_{SF}} \Big( cos(\lambda_{LP}) \cos(\lambda_{TP}) + \frac{1}{1-\nu} sin(\lambda_{LP}) sin(\lambda_{TP}) \Big) - \frac{Gb_P^2}{R} - \\ f_o &= 0 \quad \text{(EQ1)} \\ F_{TP,} &= b_p \tau cos(\beta + 30^o) + \gamma_{SF} - \frac{Gb_P^2}{2\pi d_{SF}} \Big( cos(\lambda_{LP}) cos(\lambda_{TP}) + \frac{1}{1-\nu} sin(\lambda_{LP}) sin(\lambda_{TP}) \Big) - \frac{Gb_P^2}{R} - \\ f_o &= 0 \quad \text{(EQ2)} \end{split}$$

Where  $F_{LP}$ : total force acting on the leading partial;  $F_{TP}$ : total force acting on the trailing partial;  $\gamma_{SF}$ : stacking fault energy created inside the precipitate;  $\gamma_{APB}$ : antiphase boundary energy created inside the precipitate; d: separation distance between the partials; G: shear modulus,  $F_{O}$ : other backward forces, not including the APB energy term.

In EQ1 and EQ2, the forward forces are positive, and the backward forces are negative. The first term accounts for the different resolved shear stresses acting on the leading and trailing partials. The second term describes the force imposed by the stacking fault formation that pulls the leading partial backward and pushes the trailing partial forward.

The third term accounts for the interaction between the leading and the trailing partials. The fourth term is the line tension energy term imposed by the precipitate pinning. The last term describes the other backward forces that do not include the APB energy term and the line tension energy term. By subtracting E1 from E2, we obtain the equation for the stacking fault width for Type 1 configuration, similar to the equation reported in [81].

$$d_{SF} = \frac{\left(\cos(\lambda_{LP})\cos(\lambda_{TP}) + \frac{1}{1-\nu}\sin(\lambda_{LP})\sin(\lambda_{TP})\right)Gb_P^2}{\pi[2\gamma_{SF} - b_p\tau(\cos(30^o - \beta) - \cos(\beta + 30^o))]} \quad (EQ3)$$

For edge dislocations, EQ3 is simplified into:

$$d_{SF} = \frac{\left(-\frac{1}{4} + \frac{3}{4(1-\nu)}\right) Gb_P^2}{\pi[2\gamma_{SF} - b_p \tau(\cos(30^o - \beta) - \cos(\beta + 30^o))]}$$
(EQ4)

The parameters in EQ3 are provided by the MD results and the MD potential. The MD calculates the  $\gamma_{SF}$  of the stacking fault created inside the precipitate to be 62.8 mJ/m². The shear modulus, G, and the Poisson ratio,  $\nu$ , are calculated from the elastic constants provided by the MD potential, to be 77.142 GPa and 0.338, respectively. The magnitude of the Burgers vector partial is calculated to be 0.145 nm.

EQ3 and EQ4 describe a theoretical equilibrium stacking fault width created inside the precipitate for type 1. In type 1 configuration, EQ3 shows that the stacking fault width depends primarily on the SF energy and the difference between the resolved shear stresses of the partials. The difference in the partials' stresses can be described by the angle  $\beta$ . For example, the ratio between the  $\tau_{LP}$  and  $\tau_{TP}$  are 1.0 and 2.0 for  $\beta$  of 0° and 30°, respectively. Using the provided values and EQ3, Figure 15 plots theoretical equilibrium stacking fault width created inside the precipitate as a function of the applied shear stress for different  $\beta$  angles. As shown in the figure, the  $\beta$  angles, equivalently the partials' resolved shear stress differences, significantly influences the stresses required to maintain a certain stacking fault width.

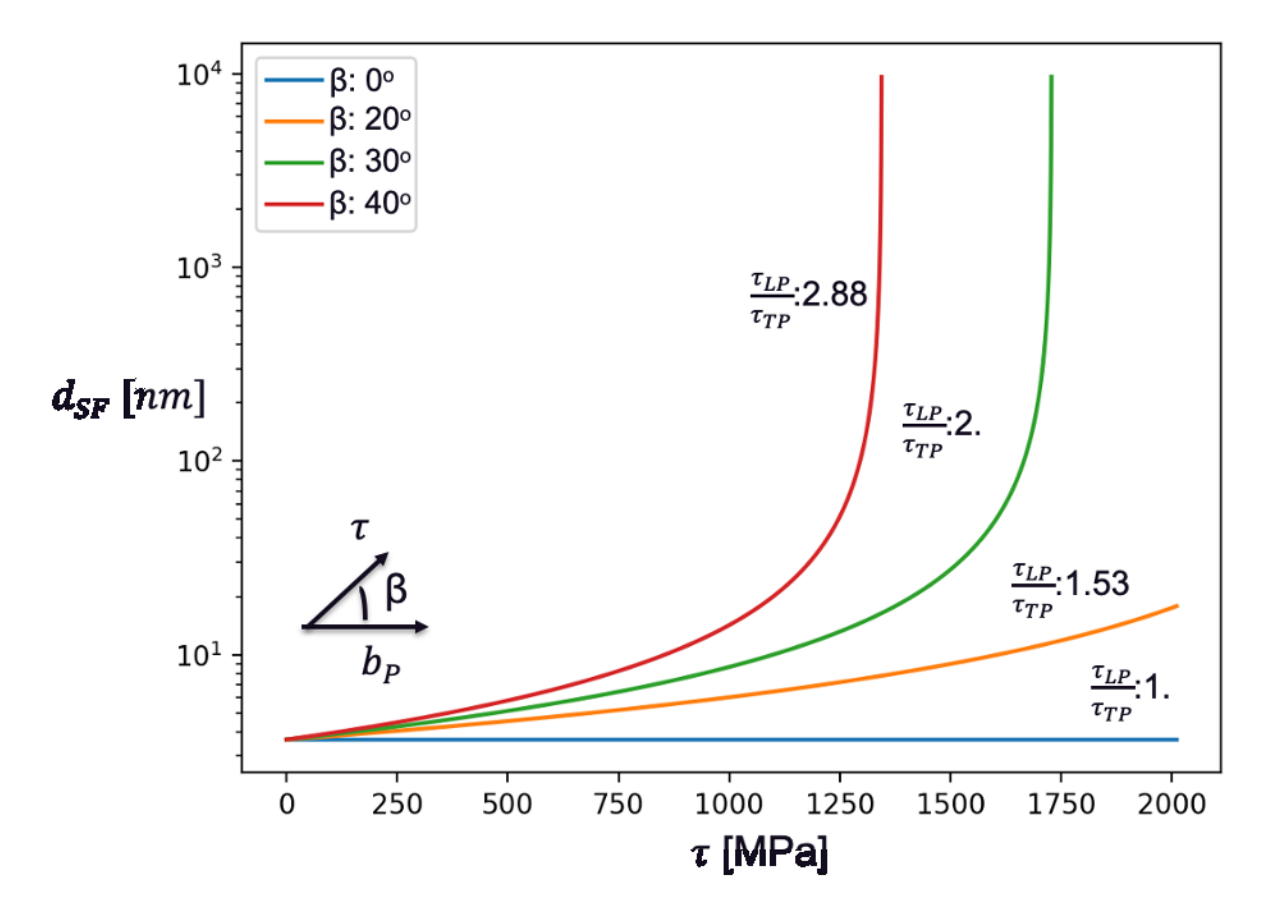


Figure 15. The theoretical equilibrium stacking fault width as a function of applied shear stress at different  $\beta$  angles. As shown in Figure 14,  $\beta$  describes the angle between the applied shear stress and the perfect Burger vector. Therefore,  $\beta$  influences the difference between the resolved shear stresses of the leading and trailing partials.

In type 2 configuration, an additional resisting force results from the antiphase boundary formation is added in EQ2. Therefore, EQ2 is modified to be:

$$\begin{split} F_{TP,} &= b_{p}\tau\cos(\beta + 30^{o}) + \gamma_{SF} - \frac{Gb_{P}^{2}}{2\pi d}\Big(\cos(\lambda_{LP})\cos(\lambda_{TP}) + \frac{1}{1-\nu}\sin(\lambda_{LP})\sin(\lambda_{TP})\Big) - \frac{Gb_{P}^{2}}{R} - \\ \gamma_{APB} - f_{o} &= 0 \text{ (EQ5)} \end{split}$$

For type 2 configuration, by subtracting EQ1 from EQ5, the stacking fault width for an edge dislocation is then written as:

$$d_{SF} = \frac{\left(-\frac{1}{4} + \frac{3}{4(1-\nu)}\right) Gb_P^2}{\pi[2\gamma_{SF} - \gamma_{APB} - b_p \tau(\cos(30^o - \beta) - \cos(\beta + 30^o))]}$$
 (EQ6)

EQ6 shows that the  $\gamma_{APB}$  helps lower the applied stress required to elongate and maintain a certain stacking width. Our MD result calculates the  $\gamma_{APB}$  of the antiphase boundary created by the trailing partial to be 139.3 mJ/m². Since the  $\gamma_{APB}/\gamma_{SF} > 2.0$ , this means that it is always preferred for the stacking fault to form and elongate when the dislocation interacts with the precipitate. However, it assumes that the ordered precipitate is infinitely large. For the finite ordered precipitate size, we observed that the stress difference between the partials play a role in determining the deformation mode, as shown in experiment and modeling. In micropillar set 2, dislocation slip takes place when the Schmid factors of the partials are similar while deformation twinning takes place when the Schmid factor of the trailing partial is a lot lower than that of the leading partial, as shown in Table 3. A similar observation was made for the stacking fault formation in the MD results. Nevertheless, this exercise allowed us to conceptualize how the APB formation helps to lower the stress required for elongating the stacking fault and the role of resolved shear stresses acting on dislocation partials in activating different deformation modes.

## 6. Summary and Conclusions

In this study, we explored the different possible interactions between the dislocations and Pt<sub>2</sub>Mo-structured precipitates (Ni<sub>2</sub>Cr type) at room temperature. Since Pt<sub>2</sub>Mo-structured precipitates are used in a wide class of Ni-Cr and Ni-Cr-Mo alloys used in power generation industries [61,67], the findings reported here serve the need to further understand the deformation behaviors of these alloys. The advances made in this work are summarized as followed:

1. Molecular dynamics simulations examined type 1 and type 2 interactions. Type 1 describes the situation in which a shift of a matrix dislocation by a perfect Burger's vector on a particular slip system maintains the ordered precipitate structure while type 2 does not; thereby creating an APB. In type 1, no elongation of the ISF is observed as the dislocations do not disrupt the order of the precipitates. In type 2, the ABP energy and the resolved shear stresses on the dislocation partials determine the formation and elongation of the ISF. More importantly, the results from our work shows that the previous geometric-based approach is insufficient in explaining the activation of different deformation modes. When considering multiple OR variants, type 2 interaction is the most dominant interaction and is

expected to be always active during dislocation glide in the presence of multiple OR variants. In particular, the activation of slip versus twin in the Ni-based alloys containing Pt<sub>2</sub>Mo-structured precipitates is determined by the Schmids factors of the dislocation partials (i.e. grain orientations) instead of the competition between type 1 and type 2 interactions.

- 2. Micropillar compression was performed to provide direct observation of the grain orientation effect on the activation of slip versus twinning, supporting the MD results. The slip behavior was found to be highly localized while the deformation twinning behavior follows by stabilized plastic flow curve. TEM analysis confirms the presence of multiple variants and the presence of deformation twin in the Ni-based alloy contain Pt<sub>2</sub>Mo-structured precipitates.
- 3. Additionally, MD results provided a possible twin formation mechanism from an energy-based approach; thus, it confirms that the type 2 interaction between the dislocations and the Pt<sub>2</sub>Mo-structured precipitates lead to the deformation twinning in Ni-Cr type alloys.

## Acknowledgements

The authors would like to acknowledge the DOE-NEUP program DE-NE 00008767, the Department of National Nuclear Security Administration through the Nuclear Science and Security Consortium under Award Number DE-NA0003180. The authors also want to thank the Nuclear Science User Facilities enabling this research through instrument access at the UC-Berkeley facility. This research used resources provided by the Los Alamos National Laboratory Institutional Computing Program, which is supported by the U.S. Department of Energy National Nuclear Security Administration under Contract No. 89233218CNA000001. Work was performed at Los Alamos National Laboratory. Los Alamos National Laboratory is an affirmative action/equal opportunity employer, and is operated by Triad National Security, LLC for the National Nuclear Security Administration of U.S. Department of Energy under contract 89233218CNA000001. Lastly, this research is being performed using funding received from the DOE Office of Nuclear Energy's Nuclear Energy University Program, Cooperative Agreement Number DE-NE0008423 and National Science User Facility, Rapid Turnaround Experiment project #1146,

FY2018. This material is also based upon work supported by the National Science Foundation under Grant No. 1653123-DMR.

## **Data Availability**

The raw/processed data required to reproduce these findings is available from the corresponding author upon reasonable request.

#### References

- [1] H. Mughrabi, U. Tetzlaff, Microstructure and High-Temperature Strength of Monocrystalline Nickel-Base Superalloys, Adv. Eng. Mater. 2 (2000) 319–326. https://doi.org/10.1002/1527-2648(200006)2:6<319::AID-ADEM319>3.0.CO;2-S.
- [2] M. Okazaki, High-temperature strength of Ni-base superalloy coatings, Sci. Technol. Adv. Mater. 2 (2001) 357–366. https://doi.org/10.1016/S1468-6996(00)00022-X.
- [3] R.C. Reed, T. Tao, N. Warnken, Alloys-By-Design: Application to nickel-based single crystal superalloys, Acta Mater. 57 (2009) 5898–5913. https://doi.org/10.1016/j.actamat.2009.08.018.
- [4] T.M. Pollock, S. Tin, Nickel-Based Superalloys for Advanced Turbine Engines: Chemistry, Microstructure and Properties, J. Propuls. Power. 22 (2006) 361–374. https://doi.org/10.2514/1.18239.
- [5] D. Furrer, H. Fecht, Ni-based superalloys for turbine discs, JOM. 51 (1999) 14–17. https://doi.org/10.1007/s11837-999-0005-y.
- [6] E. Benini, Advances in Gas Turbine Technology, BoD Books on Demand, 2011.
- [7] Y.S. Kim, W.Y. Maeng, S.S. Kim, Effect of short-range ordering on stress corrosion cracking susceptibility of Alloy 600 studied by electron and neutron diffraction, Acta Mater. 83 (2015) 507–515. https://doi.org/10.1016/j.actamat.2014.10.009.
- [8] T. Allen, H. Burlet, R.K. Nanstad, M. Samaras, S. Ukai, Advanced Structural Materials and Cladding, MRS Bull. 34 (2009) 20–27. https://doi.org/10.1557/mrs2009.8.
- [9] E. Nembach, G. Neite, Precipitation hardening of superalloys by ordered γ'-particles, Prog. Mater. Sci. 29 (1985) 177–319. https://doi.org/10.1016/0079-6425(85)90001-5.
- [10] J. Glazer, J.W.M. Jr, Strengthening contributions of strong ordered precipitates, Philos. Mag. A. 56 (1987) 507–515. https://doi.org/10.1080/01418618708214402.
- [11] A.J. Ardell, J.C. Huang, Antiphase boundary energies and the transition from shearing to looping in alloys strengthened by ordered precipitates, Philos. Mag. Lett. 58 (1988) 189–197. https://doi.org/10.1080/09500838808214752.
- [12] A.J. Ardell, Precipitation hardening, Metall. Trans. A. 16 (1985) 2131–2165. https://doi.org/10.1007/BF02670416.
- [13] A.K. Seeger, ON THE THEORY OF RADIATION DAMAGE AND RADIATION HARDENING, Max-Planck-Inst. fur Metallforschung, Stuttgart; Technischen Hochschule, Stuttgart, 1959. https://www.osti.gov/biblio/4280209 (accessed May 20, 2020).
- [14] D.J. Bacon, U.F. Kocks, R.O. Scattergood, The effect of dislocation self-interaction on the orowan stress, Philos. Mag. J. Theor. Exp. Appl. Phys. 28 (1973) 1241–1263. https://doi.org/10.1080/14786437308227997.

- [15] M.C. Chaturvedi, Y. Han, Strengthening mechanisms in Inconel 718 superalloy, Met. Sci. 17 (1983) 145–149. https://doi.org/10.1179/030634583790421032.
- [16] D. Raynor, J.M. Silcock, Strengthening Mechanisms in  $\gamma'$  Precipitating Alloys, Met. Sci. J. 4 (1970) 121–130. https://doi.org/10.1179/msc.1970.4.1.121.
- [17] A. Harte, M. Atkinson, A. Smith, C. Drouven, S. Zaefferer, J.Q. da Fonseca, M. Preuss, The effect of solid solution and gamma prime on the deformation modes in Ni-based superalloys, Acta Mater. (2020). https://doi.org/10.1016/j.actamat.2020.04.004.
- [18] A. Kirchmayer, H. Lyu, M. Pröbstle, F. Houllé, A. Förner, D. Huenert, M. Göken, P.J. Felfer, E. Bitzek, S. Neumeier, Combining Experiments and Atom Probe Tomography-Informed Simulations on γ' Precipitation Strengthening in the Polycrystalline Ni-Base Superalloy A718Plus, Adv. Eng. Mater. n/a (n.d.) 2000149. https://doi.org/10.1002/adem.202000149.
- [19] A. Luft, Microstructural processes of plastic instabilities in strengthened metals, Prog. Mater. Sci. 35 (1991) 97–204. https://doi.org/10.1016/0079-6425(91)90002-B.
- [20] R.E. Stoltz, A.G. Pineau, Dislocation-precipitate interaction and cyclic stress-strain behavior of a γ' strengthened superalloy, Mater. Sci. Eng. 34 (1978) 275–284. https://doi.org/10.1016/0025-5416(78)90060-5.
- [21] A. -w. Zhu, Strain localization and formation of heterogeneous distribution of shearable ordered precipitates: application to an Al–10at.%Li single crystal, Acta Mater. 46 (1998) 3211–3220. https://doi.org/10.1016/S1359-6454(97)00488-6.
- [22] A.A. Csontos, E.A. Starke, The effect of inhomogeneous plastic deformation on the ductility and fracture behavior of age hardenable aluminum alloys, Int. J. Plast. 21 (2005) 1097–1118. https://doi.org/10.1016/j.ijplas.2004.03.003.
- [23] A. Melander, Work hardening and softening in a dislocation glide plane with precipitates, Mater. Sci. Eng. 34 (1978) 235–240. https://doi.org/10.1016/0025-5416(78)90055-1.
- [24] V. Gerold, H.P. Karnthaler, On the origin of planar slip in f.c.c. alloys, Acta Metall. 37 (1989) 2177–2183. https://doi.org/10.1016/0001-6160(89)90143-0.
- [25] L. Kovarik, R.R. Unocic, J. Li, P. Sarosi, C. Shen, Y. Wang, M.J. Mills, Microtwinning and other shearing mechanisms at intermediate temperatures in Ni-based superalloys, Prog. Mater. Sci. 54 (2009) 839–873. https://doi.org/10.1016/j.pmatsci.2009.03.010.
- [26] G.B. Viswanathan, P.M. Sarosi, M.F. Henry, D.D. Whitis, W.W. Milligan, M.J. Mills, Investigation of creep deformation mechanisms at intermediate temperatures in René 88 DT, Acta Mater. 53 (2005) 3041–3057. https://doi.org/10.1016/j.actamat.2005.03.017.
- [27] H.M. Tawancy, Deformation behavior of ordered Ni-Mo and Ni-Mo-Cr alloys, Scr. Metall. Mater. 32 (1995) 2055–2060. https://doi.org/10.1016/0956-716X(95)00054-Y.
- [28] W. He, R. Hu, Y. Wu, X. Gao, J. Yang, Mechanical properties of an aged Ni-Cr-Mo alloy and effect of long-range order phase on deformation behavior, Mater. Sci. Eng. A. 731 (2018) 29–35. https://doi.org/10.1016/j.msea.2018.06.032.
- [29] M. Kumar, V.K. Vasudevan, Mechanical properties and strengthening of a Ni □ 25Mo □ 8Cr alloy containing Ni2(Mo,Cr) precipitates, Acta Mater. 44 (1996) 4865–4880. https://doi.org/10.1016/S1359-6454(96)00092-4.
- [30] H.M. Tawancy, M.O. Aboelfotoh, Mechanical properties of ground state structures in substitutional ordered alloys: High strength, high ductility and high thermal stability, Mater. Sci. Eng. A. 603 (2014) 121–128. https://doi.org/10.1016/j.msea.2014.02.085.

- [31] H.M. Tawancy, M.O. Aboelfotoh, High strength and high ductility in a nanoscale superlattice of Ni2(Cr,Mo) deformable by twinning, Scr. Mater. 59 (2008) 846–849. https://doi.org/10.1016/j.scriptamat.2008.06.026.
- [32] Y.L. Lu, L.M. Pike, C.R. Brooks, P.K. Liaw, D.L. Klarstrom, Strengthening domains in a Ni–21Cr–17Mo alloy, Scr. Mater. 56 (2007) 121–124. https://doi.org/10.1016/j.scriptamat.2006.09.011.
- [33] B.C. De Cooman, Y. Estrin, S.K. Kim, Twinning-induced plasticity (TWIP) steels, Acta Mater. 142 (2018) 283–362. https://doi.org/10.1016/j.actamat.2017.06.046.
- [34] Y.H. Jo, S. Jung, W.M. Choi, S.S. Sohn, H.S. Kim, B.J. Lee, N.J. Kim, S. Lee, Cryogenic strength improvement by utilizing room-temperature deformation twinning in a partially recrystallized VCrMnFeCoNi high-entropy alloy, Nat. Commun. 8 (2017) 15719. https://doi.org/10.1038/ncomms15719.
- [35] K.J. Hemker, W.N. Sharpe, Microscale Characterization of Mechanical Properties, Annu. Rev. Mater. Res. 37 (2007) 93–126. https://doi.org/10.1146/annurev.matsci.36.062705.134551.
- [36] M.D. Uchic, D.M. Dimiduk, J.N. Florando, W.D. Nix, Sample Dimensions Influence Strength and Crystal Plasticity, Science. 305 (2004) 986–989. https://doi.org/10.1126/science.1098993.
- [37] D. Kiener, P. Hosemann, S.A. Maloy, A.M. Minor, *In situ* nanocompression testing of irradiated copper, Nat. Mater. 10 (2011) 608–613. https://doi.org/10.1038/nmat3055.
- [38] P. Hosemann, Small-scale mechanical testing on nuclear materials: bridging the experimental length-scale gap, Scr. Mater. 143 (2018) 161–168. https://doi.org/10.1016/j.scriptamat.2017.04.026.
- [39] Z.W. Shan, J. Li, Y.Q. Cheng, A.M. Minor, S.A. Syed Asif, O.L. Warren, E. Ma, Plastic flow and failure resistance of metallic glass: Insight from in situ compression of nanopillars, Phys. Rev. B. 77 (2008) 155419. https://doi.org/10.1103/PhysRevB.77.155419.
- [40] M.D. Uchic, P.A. Shade, D.M. Dimiduk, Plasticity of Micrometer-Scale Single Crystals in Compression, Annu. Rev. Mater. Res. 39 (2009) 361–386. https://doi.org/10.1146/annurev-matsci-082908-145422.
- [41] J.R. Greer, J.Th.M. De Hosson, Plasticity in small-sized metallic systems: Intrinsic versus extrinsic size effect, Prog. Mater. Sci. 56 (2011) 654–724. https://doi.org/10.1016/j.pmatsci.2011.01.005.
- [42] S. Korte, W.J. Clegg, Micropillar compression of ceramics at elevated temperatures, Scr. Mater. 60 (2009) 807–810. https://doi.org/10.1016/j.scriptamat.2009.01.029.
- [43] C.D. Judge, C. Howard, V. Bhakhri, C. Dixon, C. Mayhew, S. Hoendermis, Coupling Multi-Scale Mechanical Testing Techniques with FIB and TEM Characterization to Reveal Mechanisms of Embrittlement of High Dose Inconel X-750, Microsc. Microanal. 25 (2019) 1586–1587. https://doi.org/10.1017/S1431927619008663.
- [44] C. Howard, C.D. Judge, P. Hosemann, Applying a new push-to-pull micro-tensile testing technique to evaluate the mechanical properties of high dose Inconel X-750, Mater. Sci. Eng. A. 748 (2019) 396–406. https://doi.org/10.1016/j.msea.2019.01.113.
- [45] M.D. Uchic, D.M. Dimiduk, J.N. Florando, W.D. Nix, Sample Dimensions Influence Strength and Crystal Plasticity, Science. 305 (2004) 986–989. https://doi.org/10.1126/science.1098993.

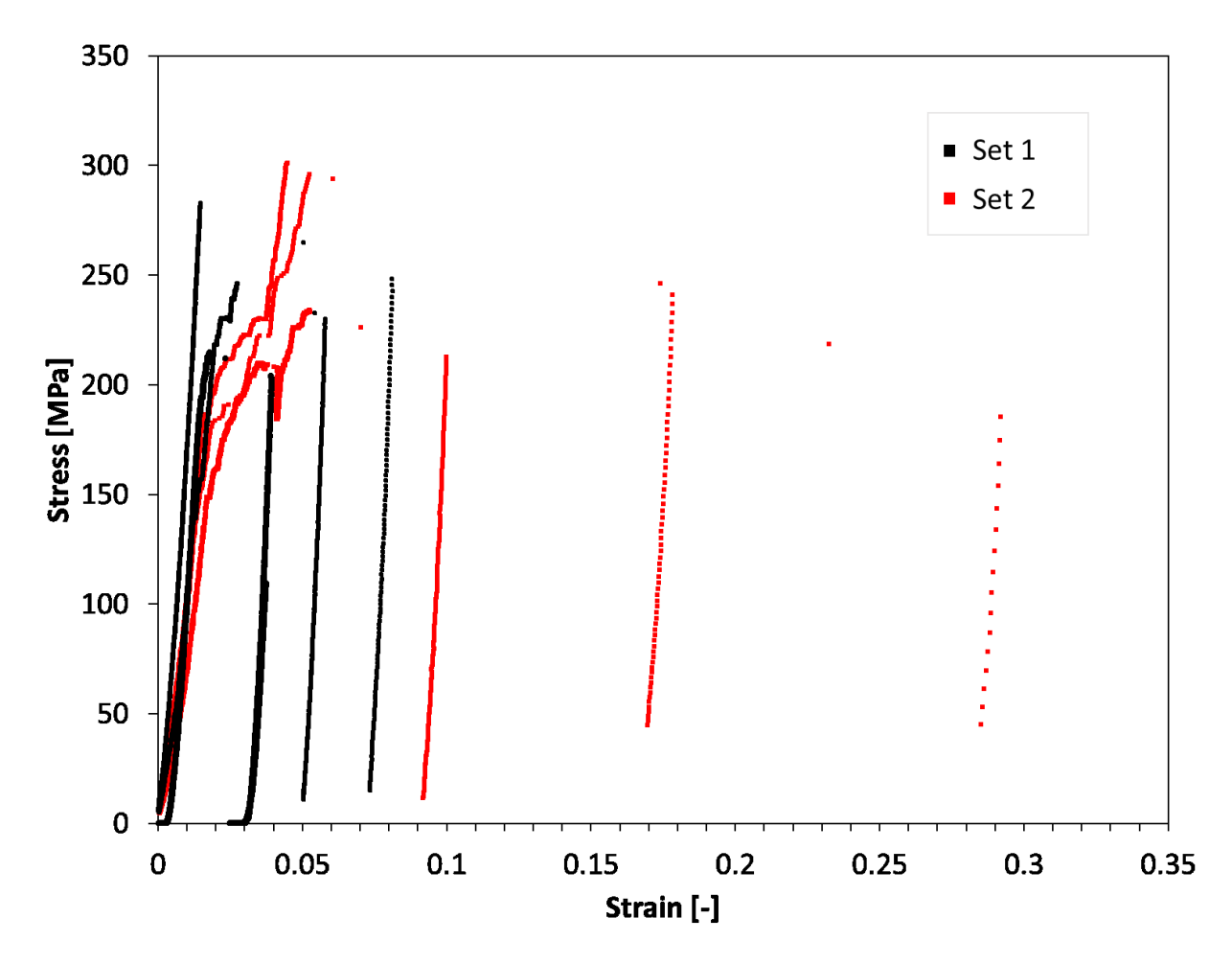
- [46] H. Tang, K.W. Schwarz, H.D. Espinosa, Dislocation escape-related size effects in single-crystal micropillars under uniaxial compression, Acta Mater. 55 (2007) 1607–1616. https://doi.org/10.1016/j.actamat.2006.10.021.
- [47] J.R. Greer, W.D. Nix, Nanoscale gold pillars strengthened through dislocation starvation, Phys. Rev. B. 73 (2006) 245410. https://doi.org/10.1103/PhysRevB.73.245410.
- [48] D.S. Gianola, C. Eberl, Micro- and nanoscale tensile testing of materials, JOM. 61 (2009) 24. https://doi.org/10.1007/s11837-009-0037-3.
- [49] G. Dehm, Miniaturized single-crystalline fcc metals deformed in tension: New insights in size-dependent plasticity, Prog. Mater. Sci. 54 (2009) 664–688. https://doi.org/10.1016/j.pmatsci.2009.03.005.
- [50] R. Dou, B. Derby, A universal scaling law for the strength of metal micropillars and nanowires, Scr. Mater. 61 (2009) 524–527. https://doi.org/10.1016/j.scriptamat.2009.05.012.
- [51] A. Rinaldi, P. Peralta, C. Friesen, K. Sieradzki, Sample-size effects in the yield behavior of nanocrystalline nickel, Acta Mater. 56 (2008) 511–517. https://doi.org/10.1016/j.actamat.2007.09.044.
- [52] C.R. Mayer, L.W. Yang, S.S. Singh, J. Llorca, J.M. Molina-Aldareguia, Y.L. Shen, N. Chawla, Anisotropy, size, and aspect ratio effects on micropillar compression of AlSiC nanolaminate composites, Acta Mater. 114 (2016) 25–32. https://doi.org/10.1016/j.actamat.2016.05.018.
- [53] H.T. Vo, A. Reichardt, D. Frazer, N. Bailey, P. Chou, P. Hosemann, In situ micro-tensile testing on proton beam-irradiated stainless steel, J. Nucl. Mater. 493 (2017) 336–342. https://doi.org/10.1016/j.jnucmat.2017.06.026.
- [54] D.M. Dimiduk, C. Woodward, R. LeSar, M.D. Uchic, Scale-Free Intermittent Flow in Crystal Plasticity, Science. 312 (2006) 1188–1190. https://doi.org/10.1126/science.1123889.
- [55] F.F. Csikor, C. Motz, D. Weygand, M. Zaiser, S. Zapperi, Dislocation Avalanches, Strain Bursts, and the Problem of Plastic Forming at the Micrometer Scale, Science. 318 (2007) 251–254. https://doi.org/10.1126/science.1143719.
- [56] M.-C. Miguel, A. Vespignani, S. Zapperi, J. Weiss, J.-R. Grasso, Intermittent dislocation flow in viscoplastic deformation, Nature. 410 (2001) 667–671. https://doi.org/10.1038/35070524.
- [57] A. Reichardt, M. Ionescu, J. Davis, L. Edwards, R.P. Harrison, P. Hosemann, D. Bhattacharyya, In situ micro tensile testing of He+2 ion irradiated and implanted single crystal nickel film, Acta Mater. 100 (2015) 147–154. https://doi.org/10.1016/j.actamat.2015.08.028.
- [58] X.W. Gu, C.N. Loynachan, Z. Wu, Y.-W. Zhang, D.J. Srolovitz, J.R. Greer, Size-Dependent Deformation of Nanocrystalline Pt Nanopillars, Nano Lett. 12 (2012) 6385–6392. https://doi.org/10.1021/nl3036993.
- [59] D. Jang, J.R. Greer, Size-induced weakening and grain boundary-assisted deformation in 60 nm grained Ni nanopillars, Scr. Mater. 64 (2011) 77–80. https://doi.org/10.1016/j.scriptamat.2010.09.010.
- [60] S. Guo, D. Xu, Y. Liang, Y. Li, J. Yang, G. Chen, D.D. Macdonald, Corrosion Characteristics of Typical Ni–Cr Alloys and Ni–Cr–Mo Alloys in Supercritical Water: A Review, Ind. Eng. Chem. Res. 59 (2020) 18727–18739. https://doi.org/10.1021/acs.iecr.0c04292.

- [61] M. Song, Y. Yang, M. Wang, W. Kuang, C.R. Lear, G.S. Was, Probing long-range ordering in nickel-base alloys with proton irradiation, Acta Mater. 156 (2018) 446–462. https://doi.org/10.1016/j.actamat.2018.06.043.
- [62] M. Sundararaman, L. Kumar, G.E. Prasad, P. Mukhopadhyay, S. Banerjee, Precipitation of an intermetallic phase with Pt2Mo-type structure in alloy 625, Metall. Mater. Trans. A. 30 (1999) 41–52. https://doi.org/10.1007/s11661-999-0194-6.
- [63] L. Yuan, R. Hu, J. Li, Evolution behavior of superlattice phase with Pt2Mo-type structure in Ni-Cr-Mo alloy with low atomic Mo/Cr ratio, J. Mater. Res. 31 (2016) 427–434. https://doi.org/10.1557/jmr.2016.34.
- [64] L. Yuan, X. Gao, X. Zhang, Y. Yang, Mechanical properties and Portevin-Le Châtelier effect of a Ni-Cr-Mo alloy containing ordered phase with Pt2Mo-type structure at elevated temperature, Mater. Sci. Eng. A. 680 (2017) 115–120. https://doi.org/10.1016/j.msea.2016.10.086.
- [65] C.S. Hong, N.R. Tao, K. Lu, X. Huang, Grain orientation dependence of deformation twinning in pure Cu subjected to dynamic plastic deformation, Scr. Mater. 61 (2009) 289– 292. https://doi.org/10.1016/j.scriptamat.2009.04.006.
- [66] R.J. McCabe, I.J. Beyerlein, J.S. Carpenter, N.A. Mara, The critical role of grain orientation and applied stress in nanoscale twinning, Nat. Commun. 5 (2014) 3806. https://doi.org/10.1038/ncomms4806.
- [67] F. Teng, D.J. Sprouster, G.A. Young, J.-H. Ke, J.D. Tucker, Effect of stoichiometry on the evolution of thermally annealed long-range ordering in Ni–Cr alloys, Materialia. 8 (2019) 100453. https://doi.org/10.1016/j.mtla.2019.100453.
- [68] S. Plimpton, Fast Parallel Algorithms for Short-Range Molecular Dynamics, J. Comput. Phys. 117 (1995) 1–19. https://doi.org/10.1006/jcph.1995.1039.
- [69] C.A. Howells, Y. Mishin, Angular-dependent interatomic potential for the binary Ni–Cr system, Model. Simul. Mater. Sci. Eng. 26 (2018) 085008. https://doi.org/10.1088/1361-651X/aae400.
- [70] A. Stukowski, Visualization and analysis of atomistic simulation data with OVITO–the Open Visualization Tool, Model. Simul. Mater. Sci. Eng. 18 (2010) 015012. https://doi.org/10.1088/0965-0393/18/1/015012.
- [71] D.M. Barnett, The displacement field of a triangular dislocation loop, Philos. Mag. A. 51 (1985) 383–387. https://doi.org/10.1080/01418618508237562.
- [72] D.M. Barnett, R.W. Balluffi, The displacement field of a triangular dislocation loop a correction with commentary, 87 (2007) 943–944. https://doi.org/10.1080/09500830701601748.
- [73] K. Dang, L. Capolungo, D.E. Spearot, Nanoscale dislocation shear loops at static equilibrium and finite temperature, Model. Simul. Mater. Sci. Eng. 25 (2017). https://doi.org/10.1088/1361-651X/aa9390.
- [74] S. Melchionna, G. Ciccotti, B. Lee Holian, Hoover NPT dynamics for systems varying in shape and size, Mol. Phys. 78 (1993) 533–544. https://doi.org/10.1080/00268979300100371.
- [75] P.M. Anderson, J.P. Hirth, J. Lothe, Theory of Dislocations, Cambridge University Press, 2017.
- [76] F.R.N. Nabarro, J.P. Hirth, Dislocations in Solids, Elsevier, 2004.

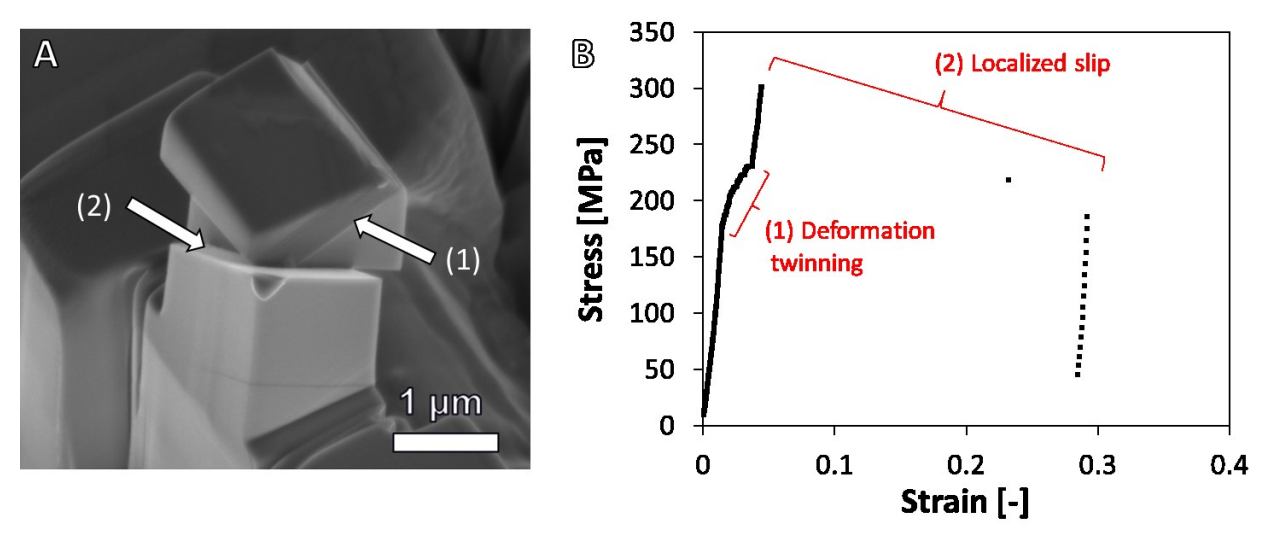
- [77] Y.T. Zhu, X.L. Wu, X.Z. Liao, J. Narayan, L.J. Kecskés, S.N. Mathaudhu, Dislocation—twin interactions in nanocrystalline fcc metals, Acta Mater. 59 (2011) 812–821. https://doi.org/10.1016/j.actamat.2010.10.028.
- [78] S. Mahajan, Critique of mechanisms of formation of deformation, annealing and growth twins: Face-centered cubic metals and alloys, Scr. Mater. 68 (2013) 95–99. https://doi.org/10.1016/j.scriptamat.2012.09.011.
- [79] J.W. Christian, S. Mahajan, Deformation twinning, Prog. Mater. Sci. 39 (1995) 1–157. https://doi.org/10.1016/0079-6425(94)00007-7.
- [80] Y.H. Zhang, Y. Zhuang, A. Hu, J.J. Kai, C.T. Liu, The origin of negative stacking fault energies and nano-twin formation in face-centered cubic high entropy alloys, Scr. Mater. 130 (2017) 96–99. https://doi.org/10.1016/j.scriptamat.2016.11.014.
- [81] T.S. Byun, On the stress dependence of partial dislocation separation and deformation microstructure in austenitic stainless steels, Acta Mater. 51 (2003) 3063–3071. https://doi.org/10.1016/S1359-6454(03)00117-4.

## **Supplementary Section**

Supplementary Figures



Supplementary Figure 1. The resolved shear stress versus strain plot of the two sets



Supplementary Figure 2. A representative set 2 micropillar, compressed to failure. Intense strain localization leads to complete failure of the micropillar along a localized slip. The

localized slip corresponds to a large strain burst while the deformation twinning shows stabilized plastic flow at the microscale level.